

High Resolution Seismic Waveform Generation using Denoising Diffusion

Andreas Bergmeister^{1,†,*}, Kadek Hendrawan Palgunadi^{2,*}, Andrea Bosisio³,
Laura Ermert², Maria Koroni², Nathanaël Perraudin^{1,†}, Simon Dirmeier¹,
Men-Andrin Meier⁴

¹Swiss Data Science Center (SDSC), ETH Zürich, Switzerland

²Swiss Seismological Service (SED), ETH Zürich, Switzerland

³Politecnico di Milano, Italy

⁴Earth and Planetary Science Department, ETH Zürich, Switzerland

[†]Work conducted while being employed at SDSC

*equal contributions

This manuscript is an arXiv preprint that has been submitted to a peer-reviewed journal and has not yet undergone peer review.

Key Points:

- A novel generative latent denoising diffusion model generates realistic synthetic seismic waveforms with frequency content up to 50 Hz.
- The model predicts peak amplitudes at least as accurately as local ground motion models, and with the same variability as in real data.
- We introduce an open-source Python library for using the pre-trained model, and to train new generative models.

Abstract

Accurate prediction and synthesis of seismic waveforms are crucial for seismic hazard assessment and earthquake-resistant infrastructure design. Existing prediction methods, such as Ground Motion Models and physics-based simulations, often fail to capture the full complexity of seismic wavefields, particularly at higher frequencies. This study introduces a novel, efficient, and scalable generative model for high-frequency seismic waveform generation. Our approach leverages a spectrogram representation of seismic waveform data, which is reduced to a lower-dimensional submanifold via an autoencoder. A state-of-the-art diffusion model is trained to generate this latent representation, conditioned on key input parameters: earthquake magnitude, recording distance, site conditions, and faulting type. The model generates waveforms with frequency content up to 50 Hz. Any scalar ground motion statistic, such as peak ground motion amplitudes and spectral accelerations, can be readily derived from the synthesized waveforms. We validate our model using commonly used seismological metrics, and performance metrics from image generation studies. Our results demonstrate that our openly available model can generate distributions of realistic high-frequency seismic waveforms across a wide range of input parameters, even in data-sparse regions. For the scalar ground motion statistics commonly used in seismic hazard and earthquake engineering studies, we show that the model accurately reproduces both the median trends of the real data and its variability. To evaluate and compare the growing number of this and similar 'Generative Waveform Models' (GWM), we argue that they should generally be openly available and that they should be included in community efforts for ground motion model evaluations.

Plain Language Summary

Predicting how the ground shakes during an earthquake is crucial for understanding earthquake hazards and for designing earthquake-resistant buildings. In this study, we use a recently developed artificial intelligence (AI) method to generate realistic, synthetic earthquake seismograms. After transforming the training seismograms from a time-domain into a time-frequency representation, we use a special type of AI model called a diffusion model—originally successful in generating images—to create synthetic seismograms. Our model takes four input parameters (earthquake magnitude, recording distance, site condition, and faulting type) and can produce any number of realistic synthetic seismograms for these parameter choices, with high-frequency details up to 50 Hz. Our study shows that the open-source model we present can create realistic seismograms in a wide variety of settings, even in areas with limited training data. For a suite of performance metrics commonly used in assessing earthquake risk and for designing safe buildings, the model closely matches the average trends and variations shown in real earthquake records. To help evaluate and compare the increasing number of such Generative Waveform Models (GWMs), we argue that such models should generally be made publicly available and included in community efforts to assess ground motion prediction models.

1 Introduction

The study and prediction of earthquake ground motions are central to seismology. Wavefield models across scales and frequencies are required to assess seismic hazard and the response of critical infrastructure to ground motion. State-of-the-art seismic hazard models use empirical ground motion models (GMMs) to estimate the expected level of ground shaking (i.e., intensity measures) at a site given an earthquake and site properties information. Other applications require the prediction of full-time histories of ground motion at sites of interest. An important example is nonlinear structural dynamic analysis and performance-based earthquake engineering (Chopra, 2007; Applied Technology Council, 2009; Smerzini et al., 2024).

Predicting ground motion is challenging, and existing methods for ground motion synthesis have specific limitations. GMMs are empirical regression models that best fit the observed data as functions of first- and second-order predictor variables, such as magnitudes, recording distances, faulting mechanisms, and site conditions (Douglas, 2003; Boore et al., 2014) and are often developed for specific regions or tectonic settings. They reduce the full wavefield to scalar properties like peak amplitudes or spectral accelerations, and are data-driven rather than physics-based, although the design of GMMs can be guided by physical considerations, e.g. via the functional form of distance-attenuation terms (Baker et al., 2021). While the different predicted variables in seismic waveforms are inherently correlated and physically linked, traditional GMMs have often considered them independently during the optimization of regression model parameters. Some more recent models account for these correlations by employing multivariate statistical techniques (Baker & Bradley, 2017; Baker et al., 2021).

State-of-the-art methods for nonlinear structural dynamic analysis and performance-based earthquake engineering require full waveforms rather than just static scalar ground motion features (Bommer & Acevedo, 2004; Luco & Bazzurro, 2007). Owing to the scarcity of available short-distance records of large-magnitude events, a common practice is to scale the amplitude spectra of existing strong-motion databases representing event magnitude, source-to-site distance, and site conditions until they meet an expected target spectrum (Baker & Allin Cornell, 2006; Katsanos et al., 2010; Aquib & Mai, 2024). These records are often sampled from relatively limited amounts of data. Notably, it is not entirely clear whether the scaling process leads to realistic waveforms and whether the true ground motion variability is accurately represented in such scaled datasets.

Wavefields can also be modeled deterministically using physics-based numerical simulations of the wave equation. However, the accuracy and spatiotemporal variability of the resulting ground motions are limited by the accuracy and resolution with which seismic wave speeds and other relevant parameters are known. Together with high computational cost, this puts modeling the full range of hazard-relevant frequencies up to 10 Hz currently out of reach, except for applications of exceptionally well-studied regions on high-performance computing systems (e.g., Rodgers et al. (2020); Paolucci, Mazzieri, et al. (2021); Touhami et al. (2022); Palgunadi et al. (2024)). As a consequence, important hazard-relevant wave propagation phenomena such as scattering, site amplification, and sedimentary basin edge effects cannot be fully accounted for, peak accelerations may be outside of the resolved frequency range, and dominant modes of structures, including the high-frequency fundamental modes of low-rise buildings, may not be captured. Computational cost and lack of detailed subsurface models also make it challenging to meaningfully account for the uncertainties in path and site effects in physics-based simulations (e.g. Mai and Beroza (2002); Savran and Olsen (2019)).

Alternatively, broadband waveforms can be modeled stochastically (Boore, 2003). The stochastic ground-motion simulation approach can generate ground motions for engineering purposes across a range of earthquakes rather than focusing solely on a single scenario. However, the limitations of this method include: (i) it is based on simplified statistical representations of source, path, and site effects, incorporating some physical concepts but lacking detailed physics of wave propagation and source mechanisms which may result in less accurate synthesis of ground motions, especially for large-magnitude earthquakes (Boore, 2003); (ii) it heavily depends on empirical parameters derived from historical earthquake data (Boore & Joyner, 1997); (iii) it assumes the phase of the seismic waves to be random (Boore, 2003; Graves & Pitarka, 2010); (iv) and it may underestimate the correlation between amplitudes at different frequencies (Bayless & Abrahamson, 2019).

Hybrid methods combine physics-based deterministic simulation at low frequencies (< 1 Hz) with stochastic simulations at high frequencies (≥ 1 Hz) (e.g., Mai et al. (2010); Graves and Pitarka (2010); Olsen and Takedatsu (2015); van Ede et al. (2020);

Jayalakshmi et al. (2021)). Classic hybrid methods can suffer from parameterization issues when extrapolating between models where the two signals are easily matched but the phase spectrum is not (Mai & Beroza, 2003; Graves & Pitarka, 2010). Hybrid models provide the opportunity to generate earthquake scenarios for a limited number of ruptures in relatively well-studied regions, typically targeting large-magnitude events and near-fault distances (e.g. Paolucci, Smerzini, and Vanini (2021)). However, they face similar challenges to those inherent to deterministic simulation, namely high computational cost and uncertainties in source characterization and seismic velocity models (Hartzell et al., 1999; Douglas & Aochi, 2008).

Some of the current limitations can potentially be overcome with machine learning techniques. In earthquake engineering, machine learning models have been used for the prediction of peak ground acceleration and response or Fourier spectra (e.g. Derras et al. (2012); Esfahani et al. (2021); Jozinović et al. (2022); Lilienkamp et al. (2022)). Alternatively, neural networks can be used to enhance simulated waveforms. For instance, Paolucci et al. (2018) generated band-limited waveforms with physics-based earthquake simulations and then trained an artificial neural network to predict and add higher frequency content via their amplitude spectra. Similarly, Gatti and Clouteau (2020) used generative adversarial networks (GAN) to extract high-frequency features from ground-motion records and use them to enhance low-frequency physics-based simulated time series, while Aquib and Mai (2024) used a combination of GAN and Fourier Neural Operator (FNO) for a similar purpose. GANs have also been used for seismic data augmentation in earthquake detection problems (Y. Li et al., 2020; Wang et al., 2021), and to train signal/noise discriminators for Earthquake Early Warning algorithms (Z. Li et al., 2018).

Conditional generative models can be designed to synthesize three-component seismic waveforms, conditional on ground motion predictor variables. Florez et al. (2022) used a Wasserstein GAN to generate realistic broadband seismograms conditional on magnitude (M 4.5–7.5), hypocentral distance ($R = 0$ –180 km), and V_{S30} (0 - 1100 m/s). Among other things, their study showed that the model accurately interpolates for conditional parameter ranges where no data may be available, but is not quite accurate for very large magnitude events ($M > 8$). Inspired by Florez et al. (2022), Esfahani et al. (2023) trained a GAN to synthesize time-frequency representations of seismograms (TFGAN) considering similar conditioning parameters (M 3.8–7.5, $R < 120$ km, $V_{S30} < 1200$ m/s). Obtaining only the amplitude part of the time-frequency response from the GAN, they utilized a phase retrieval algorithm to reconstruct the phase before transforming back to time-domain seismograms. A study by Shi et al. (2024) developed a combination of GAN and neural operators, presenting the conditional ground-motion synthesis algorithm (cGM-GANO). Their algorithm is conditioned on moment magnitude (M 4.5–8.0), closest-point-on-the-rupture to site distance ($R = 0$ –300 km), style of faulting, V_{S30} (100–1100 m/s), and tectonic environment type (subduction or shallow crustal event). The most recent study by Matsumoto et al. (2024) introduced additional input parameters focused on site-specific conditions consisting of the shear-wave velocities in the top 5, 10, and 20 m and the depth to the layer with shear-wave velocities of 1000 and 1400 m/s. They also used a modified GANs method based on pre-existing styleGAN by Karras et al. (2020). The algorithm was trained with $M > 5$, rupture distance of ≤ 100 km, and hypocentral depth of less than 30 km. For a detailed overview of the use of GAN for earthquake-related engineering fields, the reader is referred to Marano et al. (2024). While these advancements show the potential of generative waveform modeling in seismology, GAN-based models can suffer from mode collapse and other training instabilities (Goodfellow et al., 2014), and neural operators require specialized neural architectures which are not currently included in standard deep learning libraries like PyTorch.

In this study, we present a novel latent denoising diffusion model for the conditional synthesis of seismic waveforms. The model uses an autoencoder to map spectrogram rep-

representations of observed ground motions into a lower-dimensional submanifold. We train the diffusion model to generate these latent representations, rather than raw spectro- or seismograms. Our model is capable of synthesizing realistic seismic waveforms, it is straightforward and computationally economical to train, and efficient during inference. We release the code and pre-trained models as part of the 'This-Quake-Does-Not-Exist' open-source Python library and hope to instigate a community effort on open generative seismic waveform models.

The manuscript is structured as follows: in Section 2, we describe the model and training process. Data descriptions and preprocessing steps are presented in Section 3. In Section 4, we evaluate to what extent the model can generate realistic seismic waveforms, using metrics from both seismological and machine learning communities. In Section 5, we discuss the potential of our and other 'Generative Waveform Models' (GWM) for practical and scientific applications.

2 Methods

Our approach to generating high-resolution seismic waveforms with a latent diffusion model comprises three primary components. Initially, we transform the seismic waveforms into spectrogram representations, which are more amenable to generative modeling than time-domain signals. Subsequently, we employ a convolutional variational autoencoder to compress these high-dimensional spectrograms into a lower-dimensional latent space. Third, we train a denoising diffusion model based on a U-Net architecture to generate samples within this latent space, which are then mapped back to the spectrogram representation and converted to waveforms during inference. In this section we provide a comprehensive description of each component of the generative pipeline (Figure 1). Detailed explanations of the neural network architectures, which we omit here for brevity, are given in Appendix A1.

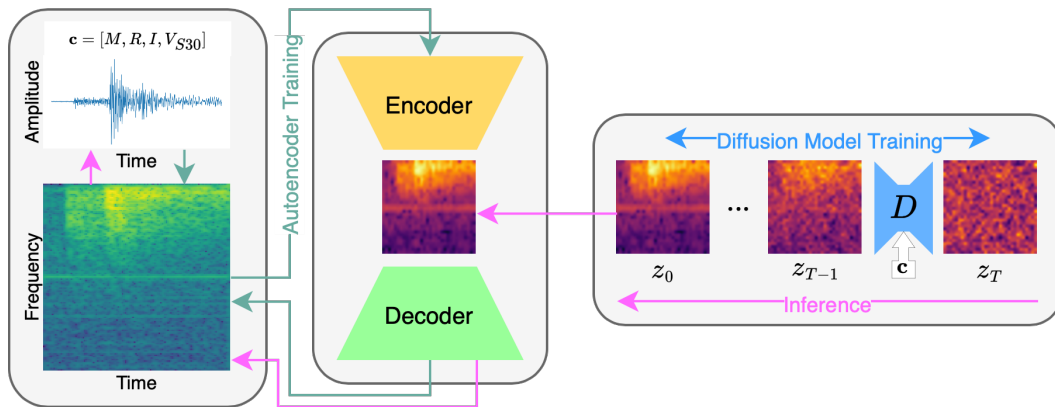


Figure 1: **Generative pipeline:** Waveforms are converted to spectrograms and an autoencoder is trained to compress them. A conditional denoising diffusion model is then trained to generate the autoencoder’s latent representations conditional on a low-dimensional parameter vector. During inference, samples are drawn from the denoising diffusion model for given conditioning parameters, mapped back to spectrograms using the decoder, and finally converted to waveforms.

2.1 Spectrogram Representation

Processing seismograms directly with neural networks is challenging due to their high-frequency content and amplitude variance, both within and across samples. This issue is particularly problematic in generative modeling, where high-amplitude areas dominate the loss function, compromising reconstruction accuracy in low-amplitude regions. To address these challenges, we transform the waveform into a spectrogram representation, a technique commonly used in seismology and in audio signal generation where typically waveforms of much higher frequency content are modeled (Kong et al., 2021; Défossez et al., 2023). Additional details on the spectrogram transformation and inversion process are provided in Appendix A2.

2.2 Departure to Latent Space

The stochastic nature of the training objective in denoising diffusion models (see Section 2.3), along with their iterative sampling process, makes both training and inference computationally intensive, particularly with high-dimensional data like high-frequency seismic waveforms. To mitigate this, we adopt the two-stage approach of Rombach et al. (2022). First, we train an autoencoder to compress the data into a more manageable, lower-dimensional latent space, then use denoising diffusion to generate the latent variables. This combines the autoencoder’s data compression efficiency with the generative capabilities of denoising diffusion models.

Formally, let p_{data} denote the data distribution density. We model the distribution over latent variables $\mathbf{z} \in \mathbb{R}^m$ as a mixture of Gaussians:

$$p_{\text{enc}}(\mathbf{z}) = \mathbb{E}_{p_{\text{data}}(\mathbf{x})} p_{\text{enc}}(\mathbf{z}|\mathbf{x}) = \mathbb{E}_{p_{\text{data}}(\mathbf{x})} \mathcal{N}(\mathbf{z} | \boldsymbol{\mu}_{\phi}(\mathbf{x}), \text{diag}(\boldsymbol{\sigma}_{\phi}(\mathbf{x}))). \quad (1)$$

Here, the encoder is defined by its mean and standard deviation functions $\boldsymbol{\mu}_{\phi}, \boldsymbol{\sigma}_{\phi} : \mathbb{R}^n \rightarrow \mathbb{R}^m$, parameterized by a neural network with parameters ϕ . The network has two output heads: one for the mean and one for the standard deviation. A deterministic decoder, $G_{\psi} : \mathbb{R}^m \rightarrow \mathbb{R}^n$, maps latent variables back to the original data space. The encoder and decoder are trained jointly to minimize the reconstruction loss

$$\mathbb{E}_{p_{\text{enc}}(\mathbf{z}|\mathbf{x})} \|\mathbf{x} - G_{\psi}(\mathbf{z})\|^2 \quad (2)$$

over the data distribution. Additionally, we regularize the latent space by the Kullback-Leibler divergence between the encoder distribution and a standard normal distribution. Since we employ the autoencoder solely for data compression rather than as a generative model, we set the regularization strength to a tiny value ($1e-6$) to ensure high reconstruction quality.

2.3 Denoising Diffusion

After compressing the data into a compact latent space, we employ denoising diffusion models (DDMs; Song and Ermon (2019); Ho et al. (2020); Song et al. (2021)) to generate the latent representations. DDMs have gained popularity due to their outstanding performance in tasks such as image, audio, or video generation. Unlike previous techniques, DDMs do not rely on approximate variational inference, which can produce blurry samples as in variational autoencoders (Kingma & Welling, 2014), or adversarial training, which can be unstable and suffer from mode collapse (Goodfellow et al., 2014). Additionally, they do not require restricted architectures like normalizing flows (Rezende & Mohamed, 2015).

DDMs are characterized by a pair of stochastic processes: a fixed forward noising process and a learnable backward denoising process. The forward process progressively adds noise to the data distribution until it resembles an isotropic Gaussian. Conversely,

the backward process commences from this noise distribution and aims to invert the effect of the forward process, recovering samples that approximately follow the data distribution. For conditional generation, both processes are modeled as conditional processes. We parameterize the backward process by a neural network, which is trained to predict the original sample, or equivalently the added noise, from the perturbed sample and the conditioning parameters.

Specifically, our data distribution is a mixture of distributions conditioned on the first-order properties of the waveforms (earthquake magnitude, hypocentral distance, site conditions, and faulting type), represented as a vector $\mathbf{c} \in \mathbb{R}^c$:

$$p_{\text{data}}(\mathbf{x}) = \mathbb{E}_{p_{\text{cond}}(\mathbf{c})} p_{\text{data}}(\mathbf{x}|\mathbf{c}). \quad (3)$$

We focus on modeling the conditional distributions $p_{\text{data}}(\mathbf{x}|\mathbf{c})$, assuming the conditional parameters are given at inference. For a fixed conditioning vector \mathbf{c} , we obtain a latent sample $\mathbf{z} \sim \mathbb{E}_{p_{\text{data}}(\mathbf{x}|\mathbf{c})} p_{\text{enc}}(\mathbf{z}|\mathbf{x})$ by passing a sample from the conditional data distribution $p_{\text{data}}(\mathbf{x}|\mathbf{c})$ through the stochastic encoder. We denote the corresponding noise-perturbed samples at time $0 < t \leq T$ as \mathbf{z}_t . These samples are obtained by evolving $\mathbf{z} = \mathbf{z}_0$ through the forward process described by the Itô stochastic differential equation

$$d\mathbf{z}_t = \boldsymbol{\mu}_t(\mathbf{z}_t) dt + \sigma_t d\mathbf{w}, \quad (4)$$

where $\boldsymbol{\mu}_t : \mathbb{R}^m \rightarrow \mathbb{R}^m$ is a time-dependent drift function, $\sigma_t > 0$ is a time-varying diffusion coefficient, and \mathbf{w} denotes the standard Wiener process. For sufficiently large T , this process converges to a Gaussian distribution. Synthetic data can then be generated by sampling from this Gaussian distribution and evolving the sample back to the latent representation distribution using the backward process

$$d\mathbf{z}_t = [\boldsymbol{\mu}_t(\mathbf{z}_t) - \sigma_t^2 \nabla_{\mathbf{z}_t} \log p_t(\mathbf{z}_t|\mathbf{c})] dt + \sigma_t d\bar{\mathbf{w}}, \quad (5)$$

where $\bar{\mathbf{w}}$ denotes the standard Wiener process with reversed time direction, and $p_t(\mathbf{z}_t|\mathbf{c})$ is the density of the sample \mathbf{z}_t given the conditioning \mathbf{c} . The score function $\nabla_{\mathbf{z}_t} \log p_t(\mathbf{z}_t|\mathbf{c})$ is generally intractable but can be approximated using denoising score matching loss (Vincent, 2011; Song et al., 2021).

Song et al. (2021) also identify a deterministic process with the same marginal distribution as the reverse process, characterized by the probability flow ordinary differential equation:

$$d\mathbf{z}_t = [\boldsymbol{\mu}_t(\mathbf{z}_t) - \frac{1}{2} \sigma_t^2 \nabla_{\mathbf{z}_t} \log p_t(\mathbf{z}_t|\mathbf{c})] dt. \quad (6)$$

In practice, integrating this deterministic process enables efficient sampling as simulating a stochastic process typically requires more time discretization steps.

For our GWM, we adopt the parameterizations proposed by Karras et al. (2022) which excel in image generation tasks. Specifically, we utilize their variance exploding version by setting $\boldsymbol{\mu}_t = \mathbf{0}$ and $\sigma_t = \sqrt{2t}$. The forward and backward processes are then given by

$$d\mathbf{z}_t = \sqrt{2t} d\mathbf{w}, \quad d\mathbf{z}_t = -2t \nabla_{\mathbf{z}_t} \log p_t(\mathbf{z}_t|\mathbf{c}) dt + \sqrt{2t} d\bar{\mathbf{w}}, \quad (7)$$

respectively, and the probability flow ODE becomes

$$d\mathbf{z}_t = -t \nabla_{\mathbf{z}_t} \log p_t(\mathbf{z}_t|\mathbf{c}) dt. \quad (8)$$

Integrating the forward process from time 0 to t yields the transition distribution $p_t(\mathbf{z}_t|\mathbf{z}_0, \mathbf{c}) = p_t(\mathbf{z}_t|\mathbf{z}_0) = \mathcal{N}(\mathbf{z}_t | \mathbf{z}_0, t^2 \mathbf{I})$. We can sample from this distribution by adding Gaussian noise with a variance of t^2 to the original sample \mathbf{z}_0 . For normalized data, as T becomes

sufficiently large, this distribution converges to an isotropic Gaussian with a variance of T^2 – a simple starting distribution for the reverse process. Utilizing the relationship

$$\nabla_{\mathbf{z}_t} \log p_t(\mathbf{z}_t | \mathbf{z}_0, \mathbf{c}) = \frac{\mathbf{z}_0 - \mathbf{z}_t}{t^2}$$

for the score of the transition distribution, we train a denoising model, denoted as $D_\theta : \mathbb{R}^d \times [0, T] \times \mathbb{R}^c \rightarrow \mathbb{R}^d$, to estimate the original sample \mathbf{z}_0 from its perturbed version \mathbf{z}_t given the conditioning \mathbf{c} . The score matching objective with a time-dependent weighting function $\lambda : [0, T] \rightarrow \mathbb{R}_+$ is then given by

$$\mathcal{L}(\theta) = \mathbb{E} \|D_\theta(\mathbf{z}_t, t, \mathbf{c}) - \mathbf{z}_0\|^2, \quad (9)$$

where the expectation is taken over the time t , the conditional distribution $p_{\text{cond}}(\mathbf{c})$, the distribution over the encoded latent sample \mathbf{z}_0 and its perturbed version \mathbf{z}_t . When the timestep t is sampled with positive probability for all $t \in [0, T]$, the optimal denoising model D_θ^* satisfies $\nabla_{\mathbf{z}_t} \log p_t(\mathbf{z}_t | \mathbf{c}) = (D_\theta^*(\mathbf{z}_t, t, \mathbf{c}) - \mathbf{z}_t)/t^2$ almost surely for all $t \in [0, T]$ (Vincent, 2011). We follow Karras et al. (2022) in parameterizing the loss weighting function and network preconditioning. To sample from the conditional diffusion model, we utilize a second-order Heun method using 25 steps corresponding to a total of 50 model evaluations.

We design model pipeline to synthesize three-component seismograms of 40 seconds in length, with 100 samples per second. Each record has a corresponding 4-element vector of meta-data, which we use as conditioning parameters. This includes event magnitude, hypocentral distance, the V_{S30} site condition parameter, and faulting type.

3 Data and Model Training

We use three-component strong motion waveforms recorded from 1996 to 2022 by K-NET and KiK-net stations in Japan, provided by the National Research Institute for Earth Science and Disaster Resilience (NIED, 2019). Before training our model, we preprocess the raw data by removing the scalar gain factor. We apply a causal 1 Hz Butterworth high-pass filter of order 2 and resample the data by interpolation to a common time vector to achieve a uniform sampling rate of 100 Hz. The waveforms are then truncated to 40 seconds in length, with the P-wave arrival (P-pick onset) set to approximately 5 seconds after the starting time of the trimmed waveform. We consider shallow crustal events with hypocentral depths of ≤ 25 km (classified as faulting type 1), and subduction events with depths > 25 km (classified as faulting type 0). We use all available events with magnitudes $M \geq 4.5$. The minimum and maximum station distances to the hypocenter are 1 km and 180 km, respectively. V_{S30} is available for most station metadata; we exclude all stations without V_{S30} values. The V_{S30} values range from 76 to 2100 m/s. In total, we use 197,370 three-component records.

We divide the available data into 90% for training and 10% for testing to facilitate hyperparameter tuning. Because of the limited number of observations—especially for large-magnitude earthquakes and short-distance recordings—we use all available data for model performance evaluation, except when noted otherwise. Training of our model was conducted on a single NVIDIA A100 GPU, requiring approximately 38 hours for the first-stage autoencoder and an additional 15 hours for the second-stage diffusion model.

4 Results

The design goal of the Generative Waveform Model (GWM) is to synthesize ground motion records that are statistically indistinguishable from real records, across a wide range of frequencies and conditioning parameters, namely source magnitudes, hypocentral distances, V_{S30} , and faulting type. In the following section, we discuss the extent

to which the Denoising Diffusion Model can achieve that goal and compare its outputs (i) to real data and (ii) to commonly used Ground Motion Models (GMMs). First, we compare the distributions of time-domain signal envelopes (Section 4.1) and of Fourier Amplitude Spectra (Section 4.2) between the real data and the GMM synthetics. Next, we evaluate how well the GMM predicts scalar ground motion intensity measures, in terms of prediction accuracy (Section 4.3.1), and variability (Section 4.3.2). Then we compare shaking durations of real data and GMM synthetics (Section 4.3.3), and the scaling between peak amplitude statistics and the conditioning predictor variables (Sections 4.3.5 - 4.3.7). Finally, we evaluate relative and absolute model performances for different magnitude and hypocentral distance ranges, by computing average model probabilities (Section 4.4), and performance metrics from the image generation domain (Section 4.5).

For each real seismogram, we use the trained model to produce a number of corresponding synthetic seismograms with the conditioning parameters of the real record, i.e. their magnitude, hypocentral distance, V_{S30} value and faulting type. We can then directly compare the real seismograms to their corresponding synthetic realizations (Figure 2). The GMM synthetics appear to capture the first-order characteristics of the real seismograms: they have clear P- and S-phases with realistic phase arrival time differences, as well as realistic coda wave decays. For the same conditioning parameter choices, there is a considerable amount of variability between individual realizations, for example in terms of peak amplitudes. In Section 4.3.2 we show that this variability closely matches the variability observed in the real data.

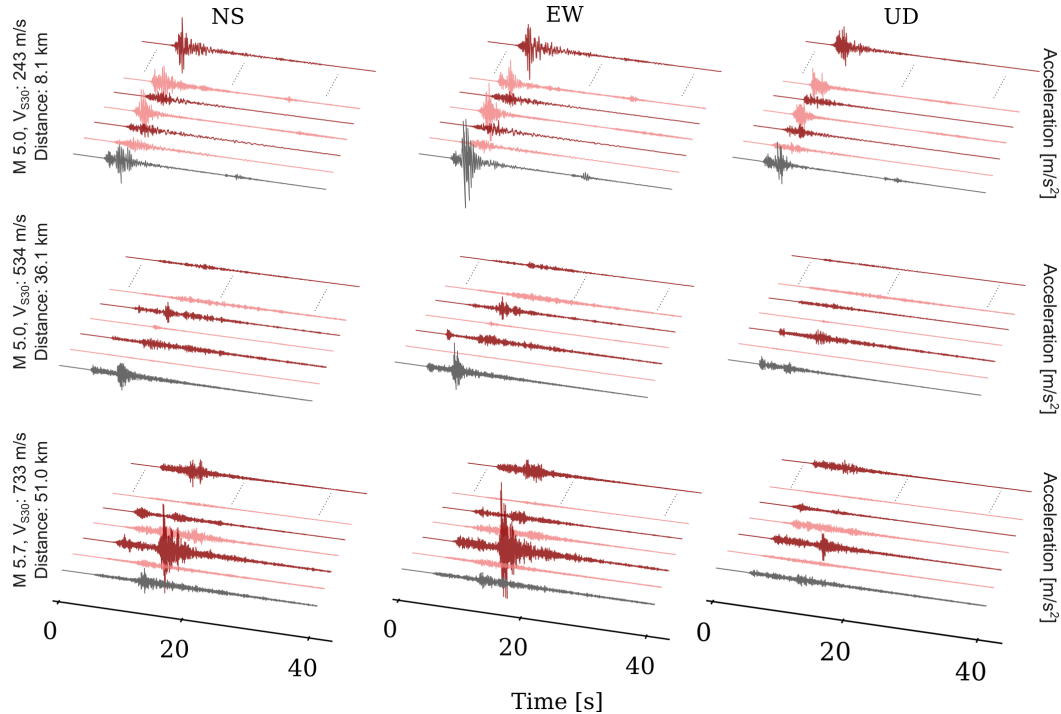


Figure 2: Real three-component acceleration seismograms (grey) and 6 randomly selected examples of GMM synthetics (red), for three sets of conditioning parameters: magnitude, hypocentral distance, V_{S30} , and faulting type values.

4.1 Time domain signal envelopes

To compare the real and synthetic waveforms quantitatively, we compute signal envelope time series for both sets. The signal envelopes are obtained by taking the moving average of the absolute waveform signals with a kernel size of 128, followed by a logarithmic transformation. This comparison shows that the GWM synthetics have very similar first-order shapes in the time domain compared to the real seismograms, across the entire range of magnitudes and recording distances for which the model was trained (Figures 3a and 3b). The low-noise amplitudes before the P-wave onsets are followed by an impulsive P-wave amplitude increase. This amplitude growth is similar for both small and large magnitudes until the smaller magnitude records reach their maximum P-wave amplitude, whereas the large magnitude records continue to grow. The later-arriving S- and surface waves cause additional amplitude growth in the real waveforms, which is accurately mimicked by the GWM synthetics. The variability of the envelopes in each bin is symmetric around the median in log-space and is of the same order for both real and synthetic data. Additional figures in the supplementary material show different bins, and separate evaluations of North-South and vertical components (supplementary Figures S1 to S7).

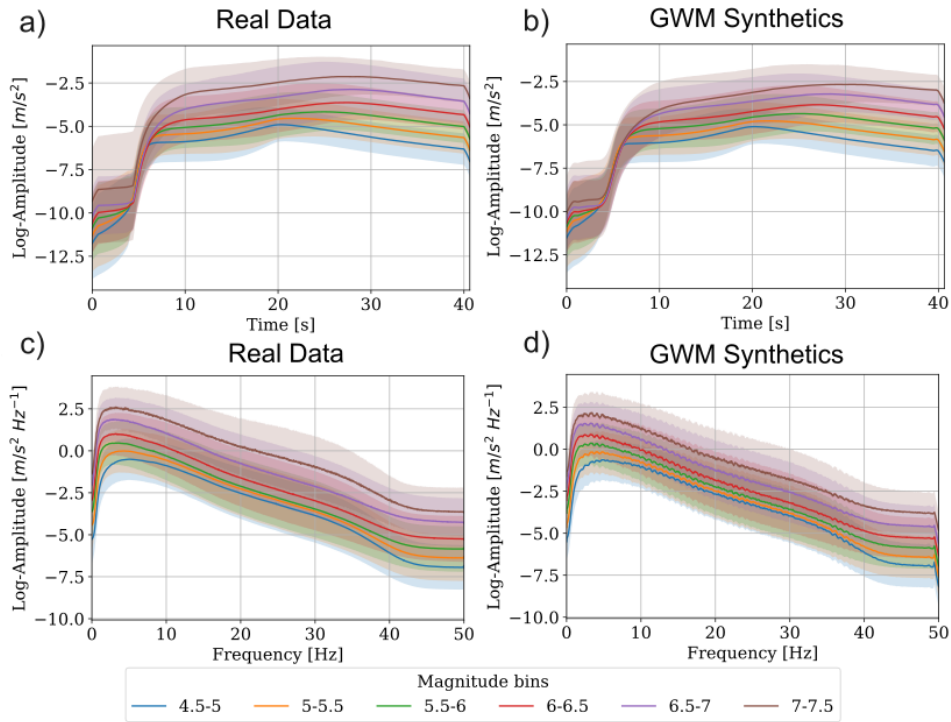


Figure 3: First order seismogram characteristics. (a) and (b) Distribution of time-domain envelopes for East-West component seismograms in different magnitude bins in terms of the mean (solid line) and the standard deviation (shaded areas) for real data and GWM synthetics. (c) and (d) Distribution of Fourier spectra log-amplitudes for East-West component seismograms in different magnitude bins. The sample counts for each bin, in ascending order of magnitude, are 58.302, 42.264, 39.033, 44.232, 13.539.

4.2 Fourier amplitude spectra

Similarly, we compare the logarithmic Fourier amplitude spectra of GWM synthetic data with those of real data. These spectra are obtained by performing a Fourier transform of the time-domain signals, calculating the magnitudes of the resulting complex values, and then applying a logarithmic transformation. Figures 3c and 3d illustrate these comparisons, with similar distributions in terms of mean log-amplitudes and variability. Equivalent evaluations for specific parameter bins are shown in supplementary Figures S2 to S7. Additionally, Section 4.5 discusses the use of Fréchet distance to compare distributions of log-amplitude spectra for real data and GWM synthetics.

4.3 Scalar peak amplitude statistics

For earthquake engineering and seismic hazard applications, peak ground motion amplitude statistics are of particular importance. Here, we compare how various peak amplitude statistics of the GWM synthetics compare with the real data, how they correlate with the conditioning predictor variables, and how they compare with predictions from widely used Ground Motion Models (GMMs). Specifically, we compute peak ground acceleration (PGA), peak ground velocity (PGV), and pseudo-spectral acceleration (SA) for both real data and GWM synthetics. We use the orientation-independent GMRotD50 statistic (Boore et al., 2006), which represents the median of the horizontal components, rotated over all possible rotation angles. We utilize GMMs from Boore et al. (2014), optimized for a global database of shallow crustal earthquakes in active tectonic regions with M 3.0–7.9 events, and from Kanno et al. (2006), which used a database of strong ground motion records from shallow crustal earthquakes in Japan between 1963 and 2003.

4.3.1 Accuracy of predicted peak amplitudes

For each record in the real waveform dataset, we compute a single GWM synthetic waveform, using the conditioning parameter of the real data (magnitude, hypocentral distance, V_{S30} and faulting type). Comparing the PGA and PGV values measured on the GWM synthetics with the real data shows that the GWM predictions are at least as accurate as those from the GMMs and have similar prediction variability (Figure 4).

Specifically, we compute the logarithm of the ratio between observed and predicted peak amplitudes. For the GWM synthetics, the mean of the distribution of this log-ratio (the model bias) is close to zero for both PGA and PGV: the mean model bias across all distances is 0.08 log-units for PGA and 0.07 log-units for PGV. This corresponds to an underprediction by 20% and 17%, respectively. At very short hypocentral distances (< 20 km), the GWM tends to underpredict the real data more strongly, by about 45% (0.16 logarithmic units, Figures 4a and 4b).

In comparison, the GMM by Boore et al. (2014) underestimates the real PGA for distances > 50 km by 21 %, and by 48 % at < 20 km (Figure 4c). For PGV, this GMM has a low average model bias of only 17 %, except at very short distances, where it is similar to the GWM (Figure 4d). Similarly, the GMM by Kanno et al. (2006) underpredicts PGA by an average of 78% (Figure 4e) across all distances and by 151% for distances < 20 km. It very accurately predicts PGV (1% under-prediction across all distances) (Figure 4f), except at short distances (< 20 km), where the under-prediction amounts to 151%. These comparisons indicate that the peak amplitude predictions of the GWM are largely unbiased, except at very short hypocentral distances where all models exhibit reduced performance.

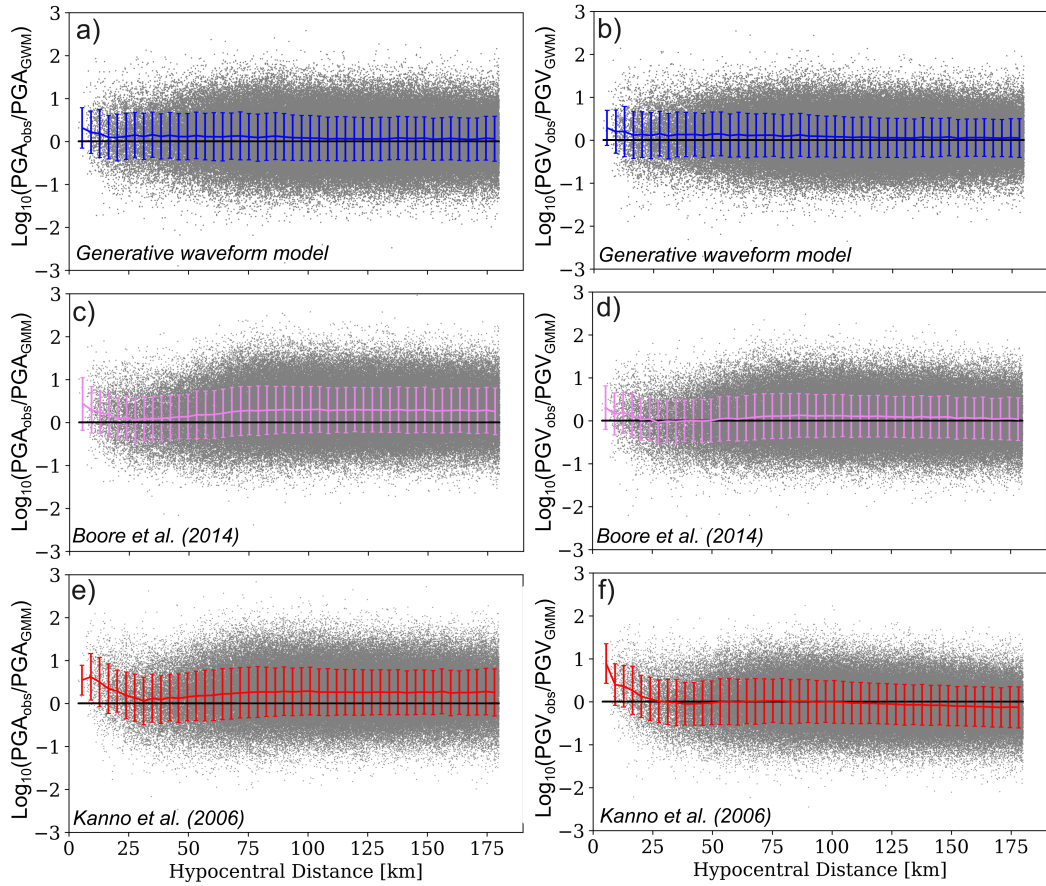


Figure 4: Model bias as a function of hypocentral distance for the generative waveform model (blue), GMMs by Boore et al. (2014) (violet), and Kanno et al. (2006) (red) for PGA (a, c, and e) and PGV (b, d, and f), with respect to real data. Colored lines represent the mean of the ratio in 50 distance bins of 3.67 km width. The bars represent the standard deviation in each bin.

4.3.2 Variability of predicted peak amplitudes

Another important criterion for ground motion prediction methods is that the variability in predicted peak amplitudes is accurately characterized. To evaluate the variability of the GWM predictions, we compare their total standard deviation to the variability in the real data, and to the predictions of the two GMMs.

To measure prediction residuals, we fit a simple, custom GMM to the PGA and PGV of the real data, as a function of magnitude M , hypocentral distance R , and V_{S30} . We use ordinary least squares and find

$$\log_{10}(\text{PGA}) = 0.4840 + 0.4274 \times M - 0.3642 \times \log_{10}(V_{S30}) - 1.3972 \times \log_{10}(R) \quad (10)$$

$$\log_{10}(\text{PGV}) = -0.9914 + 0.5392 \times M - 0.6481 \times \log_{10}(V_{S30}) - 1.3190 \times \log_{10}(R). \quad (11)$$

We then calculate residuals by subtracting the predictions of equations 10 and 11 (i) from the real data (ϵ_i^{Data}), (ii) from the GWM (ϵ_i^{GWM}), (iii) from the GMM of Boore et al. (2014) ($\epsilon_i^{\text{Boore14}}$), and (iv) from the GMM of Kanno et al. (2006) ($\epsilon_i^{\text{Kanno06}}$). The distribution of these residuals (Figure 5) is very similar between the real data and the GWM for both PGA and PGV, including extreme values. This indicates that the GWM synthetics have a similar number of waveforms with above- or below-average peak amplitudes as the real data set. The PGA residuals for the two published GMMs likewise have similar variances to the real data but are slightly shifted toward negative values. This shift reflects the larger average bias of the GMMs, as previously shown in Figure 4.

The standard deviations of the distribution of residuals are very similar for all four cases: for PGA they are 0.398, 0.399, 0.428, and 0.404 log-units, for the real data, the GWM synthetics, the Boore et al. (2014) GMM and the Kanno et al. (2006) GMM, respectively. For PGV they are 0.356, 0.357, 0.387, and 0.368, respectively. That is, for all four cases, about 68% of amplitudes fall between 40% ($10^{-0.4}$) and 251% ($10^{0.4}$) of the median predicted amplitude value.

4.3.3 Shaking durations

Shaking duration is another signal characteristic that is important for earthquake engineering applications. We use the cumulative Arias Intensity (cAI) metric (Arias, 1970) to compare the significant shaking duration of the GWM synthetics and of the real data. The significant shaking duration is defined by the times corresponding to 5% and 95% of the maximum cAI. Figure 6a shows the cAI curve for an example record from the real data set with M 5.5, recorded at $R = 50$ km, on a site with $V_{S30} = 500$ m/s, and faulting type 1, along with the cAI curves from 100 GWM realizations with the same conditioning parameters. When we compute 1 GWM realization for each real record of the entire data set (Figure 6b), we find very similar duration distributions between real data and GWM synthetics, for magnitudes ≤ 7.4 . For larger magnitudes, the 40 seconds length of the generated seismograms is not sufficient to capture the full ground motion time history. An equivalent figure that includes the largest magnitudes is given in supplementary Figure S8.

4.3.4 Predicting distributions of peak amplitudes

Because we can generate any number of synthetics with the GWM, we can use the model to predict distributions of ground motion statistics, much like we commonly would

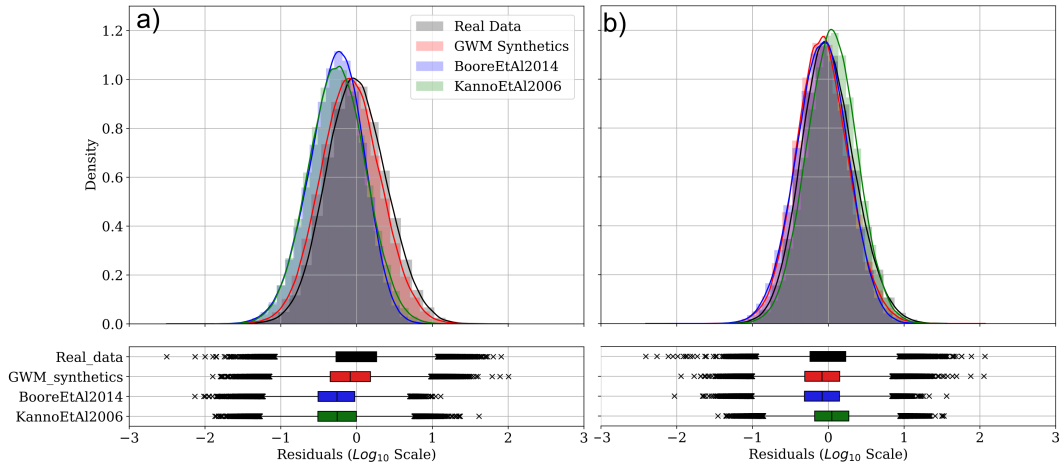


Figure 5: Histogram of (a) PGA and (b) PGV residuals showing the spread of the real data (black), of the GWM synthetics (red), of the Boore (2003) GMM (blue), and of the Kanno et al. (2006) GMM (green), with respect to the simple fitted ground motion models (equations 10 and 11) on a \log_{10} scale. The box plot shows the median values, quantiles, and extreme values.

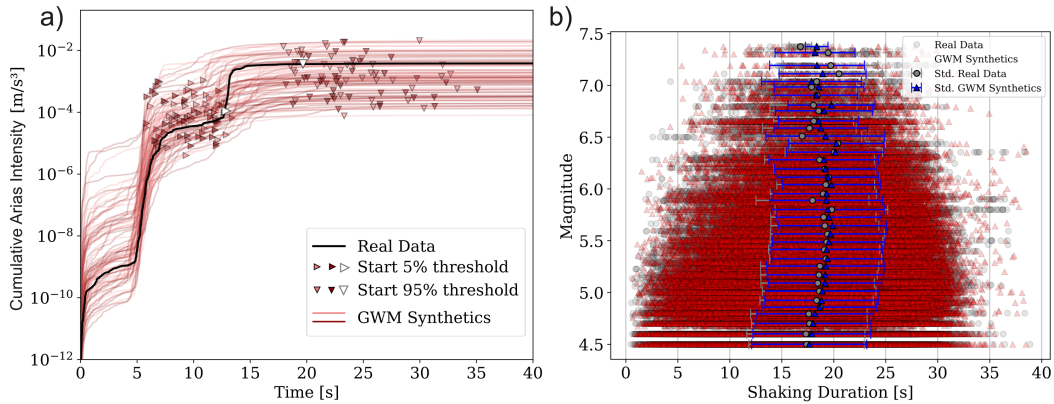


Figure 6: Shaking duration estimated using cumulative Arias Intensity (cAI). (a) cAI for a real example waveform (black line) and 100 GWM synthetics (red lines). Triangle-right and triangle-down symbols represent 5% and 95% of the maximum cAI for the real data (white) and GWM synthetics (red), respectively. (b) Shaking duration for real data (grey circles) and one GWM synthetic per real record (red triangles), with corresponding conditioning parameters. For each magnitude bin (every 0.08) from M 4.5 - 7.4, grey dots and lines show the mean and standard deviation of the real data, while blue triangles and lines show the mean and standard deviation of the GWM synthetics.

with GMMs. For instance, we can generate n synthetic waveforms for a set of conditioning parameters, and then compute the median and standard deviation of, e.g., PGA. It takes on the order of 60 GWM realizations for the median and the standard deviation estimates to stabilize (Figure 7a). To establish this we generate between 1 and 100 realizations using $M = 5.5$, $R = 50$ km, $V_{S30} = 500$ m/s, and faulting type = 1 as conditioning parameters, and analyze the median and standard deviation of the corresponding PGA values. Furthermore, we compute the Shapiro-Wilk test statistic (Figure 7b), to confirm that the peak amplitude predictions from the GWM are indeed log-normally distributed, as is the case for real data. This test statistic compares a data distribution to a normal distribution by evaluating $(\sum_{i=1}^n a_i x_{(i)})^2 / \sum_{i=1}^n (x_i - \bar{x})^2$ (i.e., the ratio between the square of the sorted weighted sample values to the sum of the squared sample deviations from the mean; where a_i is the weight and x_i is the sample). A value close to 1 indicates normally distributed data and values close to 0 imply non-normal distribution. The test values for this particular set of conditioning parameters exceed 98% at $n > 40$ and then remain stable, suggesting that the model has correctly learned to generate waveforms with log-normally distributed peak amplitudes. This is a first-order characteristic of real data, and it also implies that we can accurately represent the amplitude distributions with only a mean and a standard deviation.

4.3.5 *Pseudo-spectral acceleration versus hypocentral distance*

We can use the GWM in this sense to directly compare the distributions it predicts with predicted distributions from the GMMs. To study, for instance, how peak amplitudes decay with distance, we compute 100 GWM synthetics for a vector of evenly spaced distances, every 0.8 km between 1 km to 180 km, and calculate the median and standard deviation of the peak amplitudes in each distance bin, for fixed magnitude, V_{S30} values and faulting type (Figure 8).

For pseudo-spectral acceleration at 0.1 and 1.0 second periods with 5% damping, the resulting GWM predictions decay smoothly, similar to the GMM predictions. This includes very short distances, where both GWM and GMMs are under-constrained by available data. For $T = 0.1$ s, both the GWM and the two GMMs underestimate the real data in the $V_{S30} = 550 - 650$ m/s bin and for magnitudes in the ranges of $M = 5.4 - 5.6$ (Figure 8a) and $M = 5.9 - 6.1$ (Figure 8c), although the real data mean remains within the standard deviation of the GWM predictions. For longer periods, such as $T = 1.0$ s (Figures 8b and 8d), the GWM generally performs better than the GMMs. The GWM also matches the real data rather well in cases when the data diverge from the typical GMM decay, which is sometimes observed for distances greater than 100 km (supplementary Figures S9-S18).

4.3.6 *Pseudo-spectral acceleration versus magnitude*

In a similar sense, we can investigate how the GWM predictions grow with magnitude. We produce 100 GWM synthetics for a vector of magnitudes, evenly spaced every 0.035 from M 4.5 to 8, for a fixed distance and V_{S30} values. The predictions for SA at $T = 0.1$ s show relatively smooth, monotonous growth, up to a saturation at M 7.0 (Figure 9a), consistent with the (very sparse) real data. The same trend is observed for other conditioning parameter combinations (supplementary Figures S19 - S24). It is interesting, and encouraging, that the GWM predictions are well-behaved in conditioning parameter ranges where the training data are very sparse, such as at M 6.5 - 7.5, or for $R < 20$ km.

4.3.7 *Pseudo-spectral acceleration versus V_{S30}*

To assess the scaling of pseudo-spectral acceleration with V_{S30} , we generate another 100 GWM realizations for a vector of V_{S30} values, evenly spaced every 13.63 m/s from

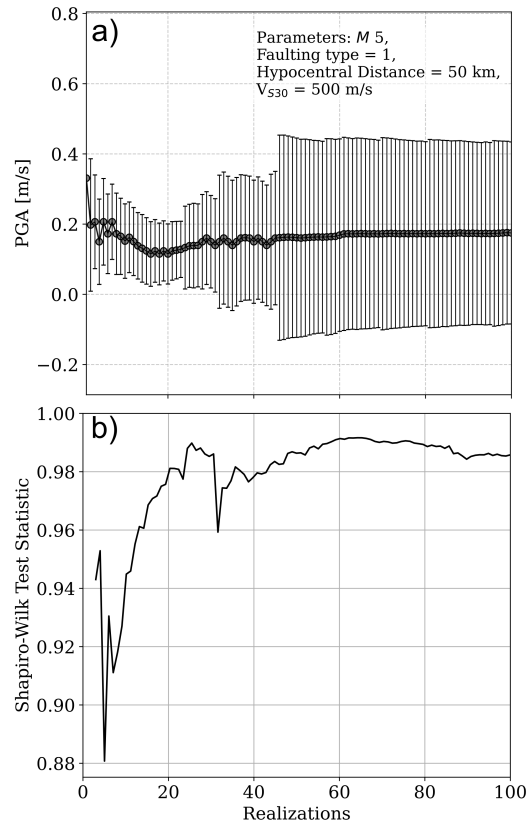


Figure 7: Statistics of the GWM realizations. a) Median and standard deviation of PGA values with different numbers of GWM realizations. b) Shapiro-Wilk test statistic for different numbers of realizations.

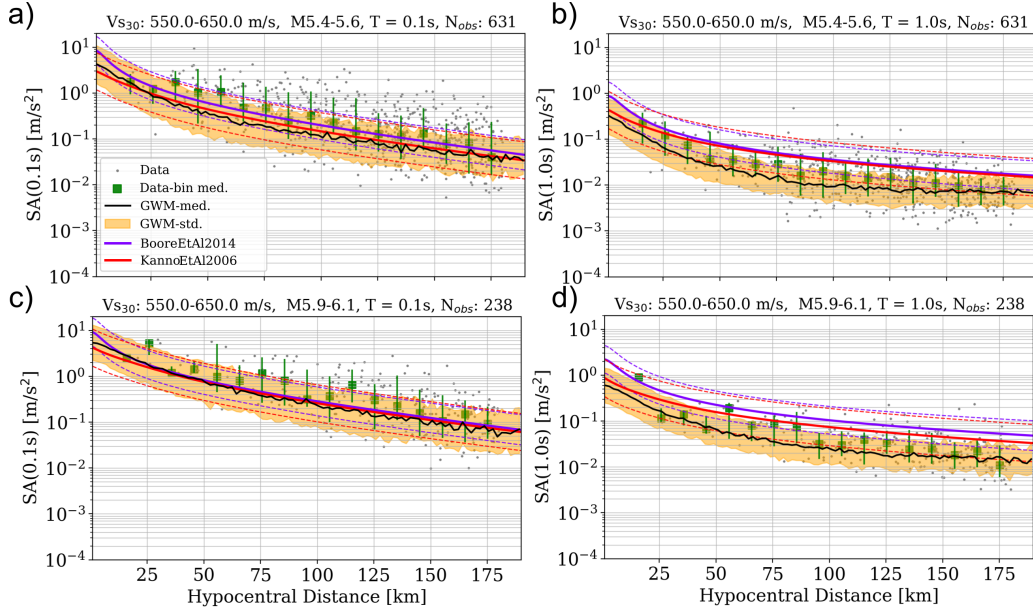


Figure 8: RotD50 pseudo-spectral acceleration (SA) with a damping factor 5% versus hypocentral distance for periods (T) of 0.1 s and 1.0 s. Median prediction of the GWM (black line) and standard deviation (yellow shaded area), along with median prediction (solid lines) and standard deviation (dashed lines) of the Boore et al. (2014) GMM (violet), and the Kanno et al. (2006) GMM (red), using $M = 5.5$ and $V_{S30} = 600$ m/s (a and b), and $M = 6.0$ and $V_{S30} = 600$ m/s (c and d). The data are sampled from narrow magnitude and V_{S30} bins, as written in the figure titles, and shown by their median (green squares) and standard deviations (green lines).

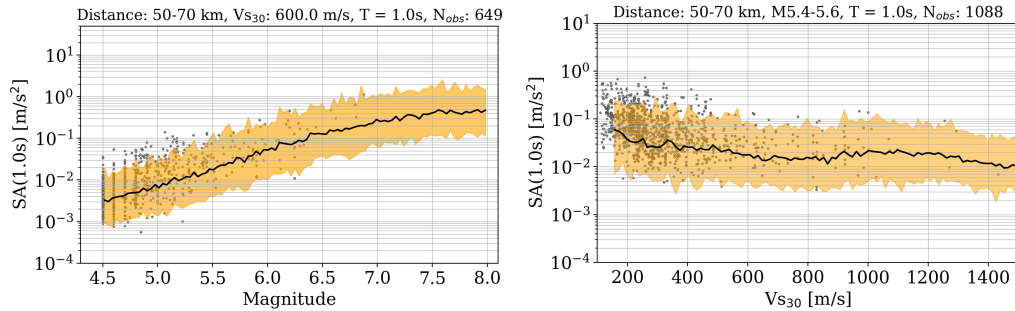


Figure 9: RotD50 pseudo-spectral acceleration (SA) with a damping factor of 5% versus magnitude (a) and versus V_{S30} (b) at $T = 1.0$ s. Median of the GWM prediction (black lines) and its standard deviation (yellow shaded areas), using $R = 60$ km, for $V_{S30} = 600$ m/s in (a) and $M = 5.5$ in (b). The data (grey dots) are sampled from narrow magnitude, R , and V_{S30} bins, as written in the figure titles.

150 m/s to 1500 m/s (Figure 9b). Generally, the GWM predictions follow the real data distribution, with SA values decreasing with increasing V_{S30} . Towards very low V_{S30} , the GWM synthetics somewhat underpredict the strong growth of SA. Interestingly, for SA at $T \geq 1.0$ s, the SA values decrease up to $V_{S30} = 800$ m/s, then remain stable up to approximately $V_{S30} = 1200$ m/s, and then decrease again for larger V_{S30} values. This is observed for a wide range of magnitude and distance bins (supplementary Figures S25-S30). To what extent we expect SA to correlate with V_{S30} somewhat depends on the known limitations of V_{S30} as a site response proxy (Bergamo et al., 2019).

4.4 Model probabilities given the data

To assess the GWM and the GMMs across a wide range of magnitude and distance combinations, we compute cumulative probabilities of the models, given the observed data. For each observed spectral acceleration value SA_i , the GWM and GMMs predict a Gaussian normal distribution of expected SA amplitudes, with a predicted mean μ , and a standard deviation σ . We can then evaluate the probability of each data point under the predicted distribution. Assuming a uniform prior distribution, this probability is equivalent to the probability of the model, given the data. By summing up these probabilities across all data points in a magnitude and distance bin, and then normalizing it with the number of data in the bin N , we can compute an average model probability

$$P^k = \frac{1}{N} \sum_i^N \frac{1}{\sqrt{2\pi}\sigma_k} \exp\left(-\frac{(SA_i - \mu_k)^2}{2\sigma_k^2}\right), \quad (12)$$

where μ_k and σ_k are the predicted mean and standard deviation for the k^{th} bin. This probability is high only if the model accurately predicts both the mean and standard deviation of the data. Therefore, with these probabilities, we can readily assess the agreement between the data and model predictions, for a large number of conditioning parameter combinations.

We compute these model probabilities for the GWM (P_{GWM}) and for the two GMMs (P_{GMM}). We use the GMMs to compute the mean SA for the center of each bin, and use their reported standard deviations. For the GWM, we use 100 GWM realizations to compute the mean and standard deviation for each bin, likewise using the magnitude and distance of each bin center. We use faulting type = 1, and repeat the computations for a number of V_{S30} values, to compute the average probabilities for each bin after Eq. 12. Figure 10 shows the model average probabilities for the GMM by Kanno et al. (2006) (top row) and the GWM (middle row). To compare the two models we compute the probability ratio $r = P_{GMM}/P_{GWM}$ (bottom row). Equivalent figures for the Boore et al. (2014) GMM are shown in supplementary Figures S31, S35, and S39.

In general, for the GWM and both GMMs, the average probabilities are highest for low magnitudes and large hypocentral distances, and lowest for large magnitudes and short recording distances. For $V_{S30} = 240$ m/s and SA with $T = 1.0$ s (Figure 10a), the GMM by Kanno et al. (2006) shows comparable accuracy to the GWM in most bins, except for $R > 100$ km. The GMM by Boore et al. (2014) is comparable to the GWM for small magnitudes and short hypocentral distances, or large magnitudes and large hypocentral distances (supplementary Figure S31a). At periods $T = 1.0$ s, the GWM performs better than any of the GMMs considered in this study (supplementary Figures S31 and S32). These patterns are also observed for higher V_{S30} values (Figures 10b,10c and supplementary Figures S33 - S40).

4.5 Fréchet Distances and classifier accuracy

In addition to the commonly used seismological performance metrics, we introduce additional, novel metrics that quantify the similarity between real and generative waveform model (GWM) synthetic waveforms. The metrics are inspired by well-established

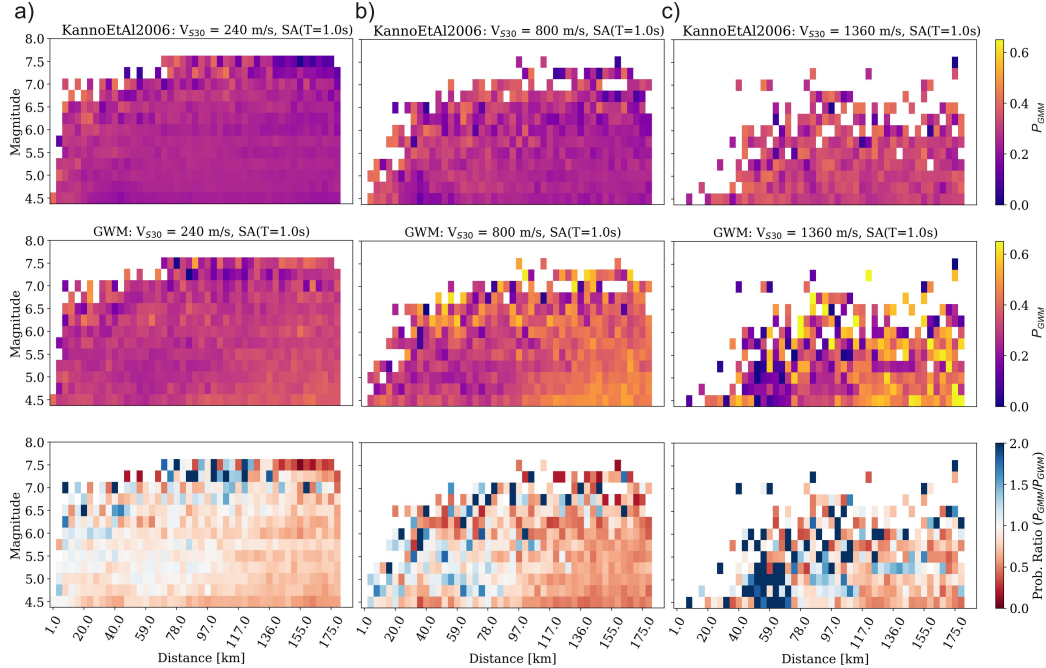


Figure 10: Average model probabilities given the SA data at $T = 1.0$ s, in bins of magnitude and R , for $V_{S30} = 240$ m/s (a), 800 m/s (b), and 1360 m/s (c), for the Kanno et al. (2006) GMM (top row) and the GWM (middle row). The ratio between the two probabilities (bottom row) shows which model explains the observed SA data better.

performance metrics from the image generation community, and could play an important role for a systematic and quantitative comparison of various proposed GWMs, e.g. in the framework of future community efforts for GWM evaluations.

4.5.1 Fréchet Distance of Fourier amplitude spectra

We use the Fréchet Distance (FD) to measure the distance between the Fourier amplitude spectra of the observed and synthetic waveforms. Ideally, realistic GWM synthetic waveforms should have a Fourier spectrum that is statistically indistinguishable from that of the real data. Larger FD values would indicate differences between the GWM synthetics and real signals. The FD is equivalent to the Wasserstein-2 distance, and measures the minimum effort required, in the L2 sense, to transform one distribution into another. As in section 4.3.1, we compute a GWM synthetic waveform for each real waveform in the data set, using the conditioning parameter corresponding to the real data. The amplitude spectrum of each waveform is represented by 2033 amplitude values ($1/2$ signal length + 1). We treat each vector element as an independent Gaussian, and compute the element-wise mean $\boldsymbol{\mu}$ and standard deviation $\boldsymbol{\sigma}$ of the log-amplitudes for each vector element, across all waveforms. The Fréchet Distance d between observed and synthetic waveforms is then given by:

$$d^2 = \|\boldsymbol{\mu}_{\text{obs}} - \boldsymbol{\mu}_{\text{syn}}\|^2 + \|\boldsymbol{\sigma}_{\text{obs}} - \boldsymbol{\sigma}_{\text{syn}}\|^2. \quad (13)$$

Computing the FD for the entire data set, we find that it ranges from 64 to 78 for the three spatial components of the seismograms (Table 1). To provide a baseline for these FD values, we also compute the FD between the training and test sets (Section 3), i.e. between sub-sets of the real data. These resulting FDs are 3 to 4 times smaller. This pro-

vides a baseline for ideal model performance, and suggests that, despite the good performance shown in sections 4.1 - 4.4, there are significant differences between real and synthetic spectra and that there is, therefore, room for model improvement. Furthermore, we also use this FD metric to show that the model performance decreases substantially if we leave out the auto-encoder, or if we choose a signal representation other than spectrograms (see ablation studies in Appendix B).

Furthermore, we can use the FD to compare the waveform generation for different magnitude and distance bins (Figure 11a and supplementary Figure S42). The FDs are systematically higher for larger magnitude and shorter distance recordings, indicating a poorer fit between real and GWM synthetic data. This may be due to the relative scarcity of training data, and/or due to the inherently higher complexity of these records, making them more challenging for a model to mimic.

Distribution	Fourier spectra FD ↓			Classifier	
	East-West	North-South	Vertical	Accuracy (%) ↑	Embedding FD ↓
GWM synthetics vs real data	77.38	64.32	71.87	44.48	5.51
Test vs training data	19.80	19.70	21.47	57.67	0.24

Table 1: Fréchet Distances (FD) of the Fourier amplitude spectra, classifier accuracies and FDs of classifier embeddings, between real data and GWM synthetics. The metrics are computed between the real data and corresponding GWM synthetics (first row), and between the training and test sets (second row).

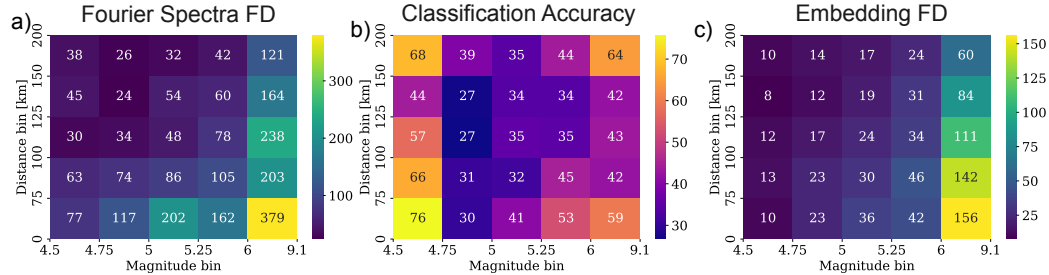


Figure 11: Fréchet Distance (FD) between real data and GWM synthetics in bins of magnitude and hypocentral distance, for the Fourier amplitude spectra of the East-West component seismograms (a), classifier accuracy on the GWM synthetics (b), and FD of the classifier embeddings between real data and GWM synthetics, in bins of magnitude and hypocentral distance (c).

4.5.2 Classification accuracy

Inspired by the common practice in image synthesis to evaluate the quality of generated images with a pre-trained classifier (Heusel et al., 2017), we adopt a similar approach: we train a classifier to categorize seismic data into bins of magnitude and distance. We divide our dataset into five magnitude and five distance bins, resulting in 25 classes, with each class containing a similar number of samples (Appendix A3). We then train a classifier to predict the magnitude-distance bin for each record. For the classifier, we use a convolutional neural network (CNN) architecture that, like the GWM, operates on spectrogram representations of the waveforms (Appendix A1). The classifier

achieves a test accuracy of 57.67%, correctly predicting the magnitude-distance bin for this fraction of real waveforms. When applied to synthetic waveforms, the classifier’s accuracy is 44.48% (Table 1). Ideally, if synthetic waveforms were indistinguishable from real ones, the classifier would maintain the same accuracy for both. Although not perfect, the classifier’s performance on synthetic waveforms strongly exceeds the $4\% = 1/25$ accuracy expected from random guessing, indicating that the synthetic waveforms encapsulate substantial information about first-order statistics, enabling the classifier to make informed predictions. Figure 11b illustrates the accuracy achieved on the generated dataset across different magnitude-distance bins. Notably, some of the most difficult parameter ranges have high classification accuracy.

4.5.3 Fréchet Distance of classifier embeddings

For similar input data, not only should the classifiers’ performance be comparable, but its internal representations should also align. Based on this intuition, we use the FD to measure the similarity of the classifiers’ hidden representations between the real and synthetic waveforms. We collect the 256-dimensional hidden representations from the penultimate layer of the classifier for both real and synthetic waveforms. Unlike the FD of Fourier amplitude spectra (Section 4.5.1) where each dimension was treated independently, the reduced dimensionality of this representation (256 instead of 2033) allows us to compute correlations between dimensions. Thus, we calculate the entire covariance matrix Σ of the hidden representations for both the real and generated waveforms. The Fréchet Distance D between the two sets of hidden representations is then given by:

$$D^2 = \|\boldsymbol{\mu}_{\text{obs}} - \boldsymbol{\mu}_{\text{gen}}\|^2 + \text{Tr}(\boldsymbol{\Sigma}_{\text{obs}} + \boldsymbol{\Sigma}_{\text{gen}} - 2(\boldsymbol{\Sigma}_{\text{obs}}\boldsymbol{\Sigma}_{\text{gen}})^{1/2}). \quad (14)$$

This is a generalization of the Fréchet Distance in Eq. 13 to general multivariate (non-isotropic) Gaussians. In image generation literature, this metric is known as the Fréchet Inception Distance (FID) (Heusel et al., 2017), with "Inception" referring to the classifier architecture employed.

This FD of classifier embeddings is about 20 times larger between the GWM synthetics and the real data, than it is between test and training data (Table 1). When computed separately for the magnitude-distance bins, we see again how the model performs worse for larger magnitude records (Figure 11c), and how the presented model performs significantly better than the ablated models evaluated in Appendix B.

In summary, all three metrics provide an objective, relative measure of synthesis quality. As such they can readily be used to e.g. compare different proposed GWMs, model versions, or to evaluate the model performance on a particular subset of the data. Importantly, ideal lower bounds for the FD, and ideal upper bounds for the classifier can be estimated by computing the metrics using just real data (second row in Table 1).

5 Discussion

Generative Waveform Models (GWMs) are rapidly advancing and have the potential to significantly improve earthquake hazard assessment and earthquake engineering studies (Florez et al., 2022; Esfahani et al., 2023; Shi et al., 2024; Matsumoto et al., 2024). Unlike GMMs, which predict scalar ground motion metrics, GWMs can synthesize fully realistic waveforms, complete with realistic frequency- and time-domain properties.

The ability to predict full waveforms enables studies that rely on waveform content, such as building response simulations (Bommer & Acevedo, 2004). Any scalar ground motion metric can be derived from the predicted waveforms. A key advantage of this approach is that the waveforms and their derivatives are equally realistic across the entire frequency range (1 - 50 Hz). This may contrast with hybrid methods, which add high-frequency spectra in a separate second stage, either using stochastic methods (Saikia &

Somerville, 1997; Mai et al., 2010; Graves & Pitarka, 2010) or neural networks (Paolucci et al., 2018; Gatti & Clouteau, 2020; Okazaki et al., 2021). The former can introduce artifacts at the transition between the deterministic and stochastic parts of the predictions (Mai & Beroza, 2003; Graves & Pitarka, 2010; Tang & Mai, 2023).

Another advantage of GWMs is their ability to accurately learn the correlation between scalar statistics of the same waveform (e.g., spectral accelerations at different frequency ranges). This factor has been considered in only a few GMMs to date (Baker & Bradley, 2017; Baker et al., 2021).

This study introduces a new GWM that builds on the recent successes of Denoising Diffusion Models in image, audio, and video generation (Song & Ermon, 2019; Ho et al., 2020; Song et al., 2021; Dhariwal & Nichol, 2021; Nichol & Dhariwal, 2021; Kong et al., 2021; Rombach et al., 2022; Ho et al., 2022). Diffusion models are capable of generating high-resolution and diverse samples while being simple to implement and train. Unlike GANs (Florez et al., 2022; Esfahani et al., 2023; Matsumoto et al., 2024) used for synthesizing waveforms, denoising diffusion models do not suffer from mode collapse or related training challenges. Additionally, no dedicated neural network architecture is required, as with neural operators (Shi et al., 2024).

The proposed GWM operates on the spectrogram representation of waveform data to address scaling issues associated with the high variance of seismic waveforms. It incorporates an autoencoder to compress these spectrograms into a more compact form, thereby enhancing the efficiency of both the training and generation processes while simultaneously improving the resolved frequency of the generated waveforms. This efficiency may also lead to better model performance in scenarios where data scarcity is a concern, a common issue in many earthquake seismology problems. Moreover, it is important for applications where large numbers of forward computations are required, such as in probabilistic seismic hazard assessment.

The proposed generative latent denoising diffusion model generates highly realistic waveforms across the entire hazard-relevant frequency range. The GWM synthetics have realistic time domain shapes (Figure 3a), Fourier amplitude spectra (Figure 3c), and shaking durations (Figure 6). The predicted peak amplitude statistics are largely unbiased (Figure 4) and have log-normally distributed amplitude variation (Figure 7), with the same amount of variability as the real data (Figure 5),

With repeated inference for the same conditioning parameter sets, GWMs can be used to predict distributions of scalar amplitude statistics, like is commonly done with GMMs. We show that our model predicts peak amplitudes of strong motion seismic data in Japan at least as accurately and as precisely as two prominent and adequate GMMs.

While GWM-based predictions are computationally more expensive than GMM computations, they offer new possibilities for both practical and scientific applications. For instance, next-generation seismic hazard models could include model branches containing a catalog of representative waveforms - rather than just amplitude statistics - which are expected over the hazard target period. This would provide a much more detailed description of the anticipated ground motion in a target region. It would also expand the applicability of hazard calculations to use cases where full waveforms are required or desirable, such as non-linear structural dynamic analyses.

GWMs could eventually eliminate the need to re-scale limited data pools of observed seismic waveforms to match expected target spectra, or to use hybrid methods for enriching simulated waveforms with high-frequency seismic energy. Instead, a set of fully realistic broadband waveforms can be generated from a single, self-consistent synthesis process.

One important question in this context will be which among existing and future GWMs generates the most realistic waveforms for a particular application. To facilitate quantitative and representative model comparisons, we propose that the emerging GWM community embrace open model and code standards and participate in existing community efforts for the comparison and evaluation of ground motion models (e.g., Maechling et al. (2015)). Performance metrics like the ones introduced in Section 4.5 could facilitate meaningful comparison between models and model versions. Such model comparison efforts could also include blind signal classification exercises, where trained classifier models would attempt to distinguish between real and synthetic waveforms.

5.1 This-Quake-Does-Not-Exist ('tqdne') Python Library

For the model presented in this study, we introduce an openly available and user-friendly Python library that can be used to generate waveforms using the pre-trained GWM from this study or to train custom GWMs. Generating a three-component waveform with the pre-trained GWMs takes a fraction of a second on a standard personal computer. The library facilitates saving of the waveforms in SeisBench format (Woollam et al., 2022). The library’s name is inspired by the popular thispersondoesnotexist.com (2023) application, which uses the StyleGAN algorithm (Karras et al., 2019, 2020) to generate human portrait images.

5.2 Limitations

While the presented GWM arguably achieves high seismic waveform synthesis performance, there are several limitations, that future models can aspire to overcome.

Stochastic nature of the generated waveforms Fundamentally, the generated waveforms are stochastic representations of real seismograms. There is no underlying physical model for wave excitation and propagation. Although the GWM synthetics exhibit clear energy packets that closely resemble P-, S- and surface waves, they do not represent any wavefield phases in a deterministic sense.

Limited training data As is the case for all models of strong ground motion, the limited number of short distance recordings of large magnitude earthquakes is a bottleneck. This limitation affects the synthesis performance of this crucial data regime. GWMs can in principle be used to augment such data sets, but it is currently an open question how well the models extrapolate beyond the parameter ranges for which they have been trained, and how well they perform at the data-scarce edges of the parameter ranges.

Point source assumption Our model assumes that the earthquake source is a point source and neglects finite fault source characteristics such as fault geometry and distance, source roughness, directivity, and unilateral or bilateral rupture modes.

Uncorrelated stations The current model does not explicitly take into account the correlation of observations across different records of the same quake. Each generated waveform is an independent realization of the denoising forward process. This may lead to an underestimation of the correlation of observed ground motions from the same quake, and might limit the ability of the model to generalize to new stations.

P-wave onset times The current model has been trained with a data set of waveforms that have been aligned with a simple STA/LTA onset detector, which can be inaccurate. As a consequence, the GWM synthetics also have some variability in the P-wave onset times that is not physically meaningful.

Signal length The 40-second long seismograms are sufficient to describe the ground motion from quakes with magnitudes of up to ~ 7.5 . For even larger quakes, the source

duration alone may exceed this signal length. Producing longer sequences without compromising temporal resolution presents some challenges, even for our efficient model. Addressing this issue may necessitate an approach with more favorable asymptotic behavior, which is a subject for future research.

Lower spectral amplitude Our model slightly underestimates the spectral amplitude of the ground motion compared to the real data (Figures 3b and 4a). This discrepancy is observed exclusively in the model operating on the spectrogram representation. We hypothesize that this is due to the model generating a slightly blurred version of the encoded spectrograms, similar to the effect of a Gaussian filter. While this blurring is inconsequential for image generation tasks, as it is imperceptible to the human eye, it may result in a lower spectral amplitude (e.g., averaging $0.04 \text{ m/s}^2\text{Hz}^{-1}$ at frequency $< 30 \text{ Hz}$, (supplementary Figure S41)). Partially, the underestimation may also stem from the spectrogram autoencoder (Figure B1c). A potential solution could involve incorporating additional loss terms, such as adversarial loss, to encourage the model to generate sharper spectrograms. These could for instance be included in the autoencoder stage. Alternatively, exploring different, potentially smoother spectral representations that are less sensitive to blurring may also be beneficial.

6 Conclusion

We present a data-driven, conditional generative model for synthesizing three-component strong motion seismograms. Our generative waveform model (GWM) combines a convolutional auto-encoder with a state-of-the-art latent denoising diffusion model, which generates encoded - rather than raw - spectrogram representations of the seismic signals.

We trained the openly available model on Japanese strong motion data with hypocentral distances of 1–180 km, moment magnitudes ≥ 4.5 , and V_{S30} values of 76–2100 m/s. Using a variety of commonly used and novel evaluation metrics, we demonstrate that the GWM synthetics accurately capture the statistical properties of the observed data in both the time and frequency domains, across a wide range of conditioning parameters, and up to the highest hazard-relevant frequencies.

Furthermore, we systematically compare the peak ground motion statistics of the GWM synthetics to predictions from commonly used GMMs. The GWM predictions are largely unbiased and exhibit the same level of amplitude variability as the real data. As a result, they may be useful for practical applications, such as probabilistic seismic hazard assessment and structural dynamic analyses.

With GWMs, hazard models can potentially expand their scope to include applications that require full waveform representations, rather than just scalar amplitude statistics. Future community efforts to benchmark and compare GWMs would provide guidance for which models to best use in practical and scientific applications, and may accelerate GWM innovation.

Appendix A Generative model details

This section provides additional details on the model architectures and representations used in the experiments.

A1 Neural network architectures

All our models are based on the widely used U-Net architecture presented in Song et al. (2021). The U-Net consists of three components which we denote *left* (encoder), *middle*, and *right* (decoder). All components use several residual blocks that use two convolutional layers (2D for the spectrogram and 1D for the moving average envelope), with

pre-layer group normalization and SiLU activation functions. In addition, the downsampling component uses a convolutional layer to reduce the dimensionality of an input between each pair of residual blocks, while the upsampling component uses upsampling operations to double the dimensionality of an input between each pair of residual blocks. An overview of the architectures is given in Table A1.

Denoising Diffusion: The neural network for the diffusion model uses four residual blocks on encoder and decoder components, with an additional residual block in the middle. After the first three levels, we include a downsampling operation on the encoder and an upsampling operation on the decoder side. In addition, the central blocks incorporate a self-attention module. As per convention, conditioning information is injected within each residual block by concatenating projections of the conditioning vector \mathbf{c} and the time embedding t to the intermediate representations of an input \mathbf{z}_t (see Figure A1 and Song et al. (2021); Karras et al. (2022)).

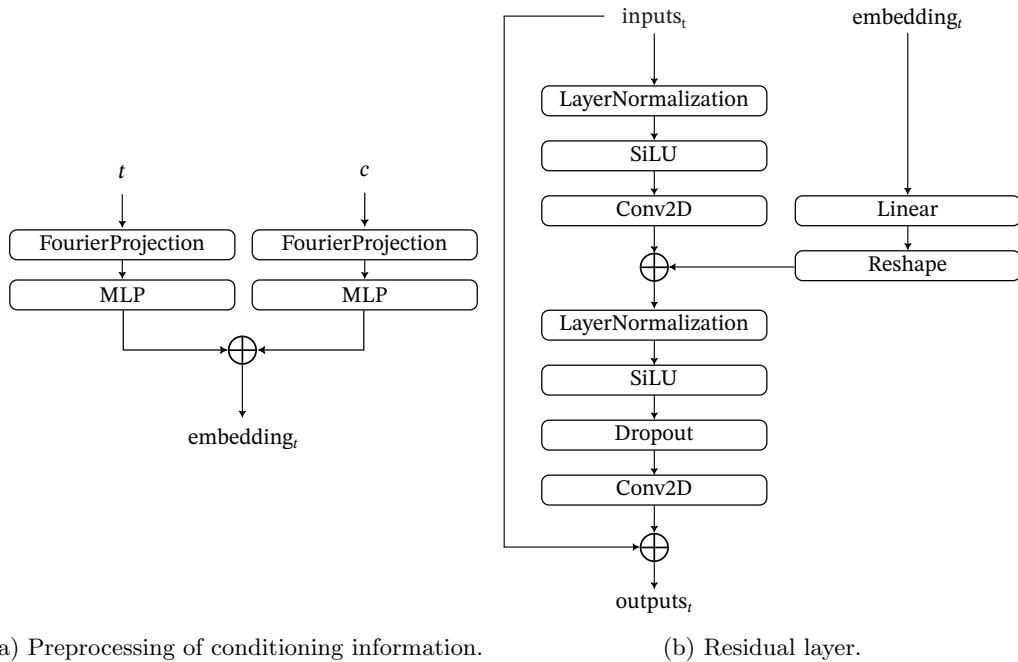


Figure A1: Using low-dimensional features for conditioning the diffusion model. (a) For both the scalar value t and the four-dimensional feature vector \mathbf{c} , we first compute 256-dimensional Fourier features and embed both via separate MLP neural networks. The two embeddings are combined by simply adding them elementwise. (b) For each residual block, we condition the synthesized spectrogram (inputs_t) using the combined time-feature embedding by adding them to the hidden representation of the residual layer. For that, we take the 256-dimensional embedding vector, transform it through a linear layer with K output neurons, and reshape it to match the size of the hidden representation. Concretely, if the hidden representation has dimensionality $N \times H \times W \times K$ where N is the batch size and $H \times W$ is the spectrogram size, we repeat the embedding $N \times H \times W$ times, reshape the resulting tensor to match the dimensionality of the hidden representation, and add the hidden representation and conditioning information elementwise (in deep learning libraries like PyTorch this can be efficiently done).

Autoencoder: The autoencoder architecture comprises the same blocks as the denoising model but lacks self-attention modules and only uses 3 residual blocks. It uses

downsampling and upsampling operations between each residual block. As a consequence, the autoencoder compresses the input by a factor of four in each spatial dimension.

Classifier: The classifier is a convolutional neural network consisting of four residual blocks, each followed by a downsampling operation. It includes a self-attention layer at the end, followed by a global average pooling operation, an output multi-layer perceptron (MLP), a linear layer, and a softmax activation function. When extracting embeddings from the classifier, we utilize the output of the MLP prior to the linear layer. The classifier is trained on the spectrogram representation of the data.

Hyperparameters	Moving Average Diffusion	Moving Average Latent Diffusion Autoencoder	Latent Diffusion Model	Spectrogram Diffusion	Spectrogram Latent Diffusion Autoencoder	Latent Diffusion Model	Classifier
Convolution Kernel Size	5	5	5	3 × 3	3 × 3	3 × 3	3 × 3
Hidden Channels	[64, 128, 256, 256]	[64, 128, 256]	[64, 128, 256, 256]	[64, 128, 256, 256]	[64, 128, 256]	[64, 128, 256, 256]	[64, 128, 256, 256]
Attention Levels	[4]	-	[4]	[4]	-	[4]	[4]
Dropout Rate	0.1	0.1	0.1	0.1	0.1	0.1	0.1
KL Weight	-	10 ⁻⁶	-	-	10 ⁻⁶	-	-
Optimizer	Adam	Adam	Adam	Adam	Adam	Adam	Adam
Learning Rate	10 ⁻⁴	10 ⁻⁴	10 ⁻⁴	10 ⁻⁴	10 ⁻⁴	10 ⁻⁴	10 ⁻⁴
EMA Decay	0.999	0.999	0.999	0.999	0.999	0.999	0.999
Batch Size	320	64	1536	320	64	2048	128
Epochs	300	200	300	300	200	300	100

Table A1: Hyperparameters for the various models used in the experiments.

A2 Representations

We experiment with two different representations of the seismic data: spectrogram and moving average envelope.

Spectrogram Representation: To transform each of the three channels in the original waveform into a spectrogram, we utilize a Short-Time Fourier Transform (STFT) with 256 frequency bins and a hop length of 32 samples. Due to the symmetry of the spectrogram, only half of the frequency bins are used. To prevent padding issues, the original waveform is truncated to 4064 samples, resulting in a complex-valued matrix of size 128×128. We then take the magnitude of this matrix and apply a logarithmic transformation to obtain the spectrogram, discarding the phase information due to its high-frequency nature, which is challenging to model accurately. To reconstruct the original waveform, we employ the Griffin-Lim algorithm (Griffin & Lim, 1984; Perraudin et al., 2013), which reliably estimates the phase from the magnitude spectrogram.

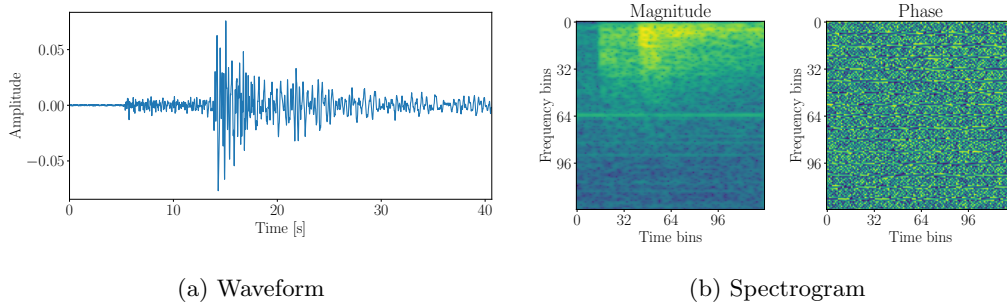


Figure A2: Seismic waveform and its corresponding spectrogram representation.

Moving Average Envelope Representation: The moving average envelope is computed by convolving the absolute waveform signal with an averaging boxcar filter

of length 128. The final representation is the concatenation of the original waveform divided by the envelope and the logarithm of the envelope.

A3 Classifier training data binning

When training the classifier to categorize data based on earthquake magnitude and distance, we divide the data into five magnitude and five distance bins. Figure A3 displays the sample count in each bin, ensuring a balanced sample distribution across classes.

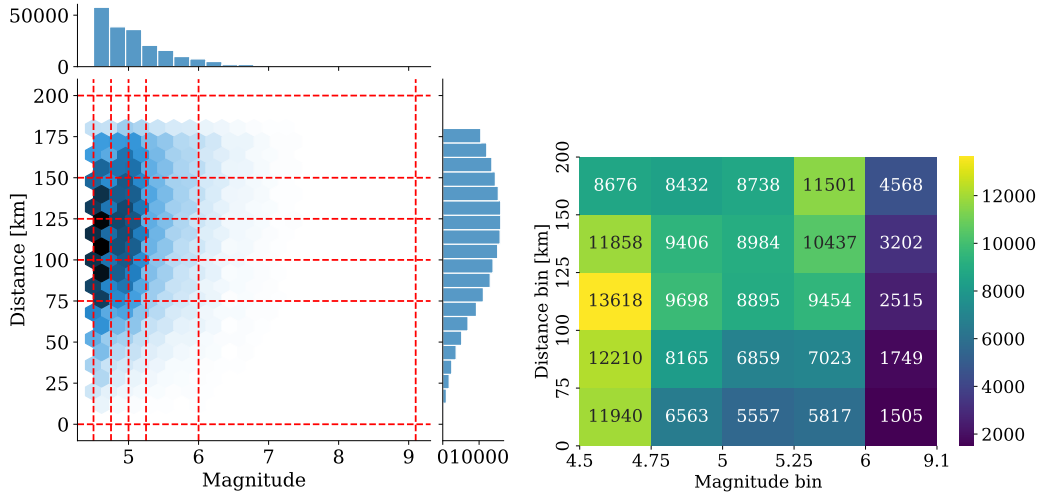


Figure A3: Binning of the data into classes for the classifier, based on magnitude and distance.

Appendix B Ablation Studies

This section evaluates the significance of the three components in our proposed model. The time-domain representation of seismic data shows significant amplitude variation, making direct processing of raw waveforms ineffective. Figure B1a illustrates the logarithm of the Fourier amplitude spectrum between an autoencoder’s input and output when trained on raw waveforms, revealing poor reconstruction, especially in the high-frequency range. It is important to note that this is not a generative model but an autoencoder tasked to reconstruct the input. Despite this, the waveforms are poorly reconstructed, particularly in the high-frequency range.

To address this, we explore alternative time-domain representations. We decompose the signal into its positive envelope and residual signal, with the envelope being a smoothed version of the absolute signal, as detailed in Section A2. Figure B1b shows that an autoencoder trained on this representation performs better than one trained on raw waveforms but still struggles with high-frequency components.

Thirdly, we experiment with a spectrogram representation, specifically the log-transformed magnitude of the short-time Fourier transform. This representation is smooth and robust to amplitude variations. Figure B1c demonstrates that an autoencoder trained on this representation nearly perfectly reconstructs the original signal, with the exception of a minor underestimation of the spectral amplitude, as discussed in Section 5. This high-

lights the effectiveness of the spectrogram representation for the task of ground motion synthesis.

Finally, we assess the performance of the diffusion model trained on different representations and the impact of incorporating the autoencoder stage. Table B1 summarizes our findings, showing that the spectrogram representation significantly outperforms the envelope representation across all metrics. Additionally, the autoencoder stage improves the spectral fit. Overall, the latent diffusion approach with the spectrogram representation is the most effective configuration.

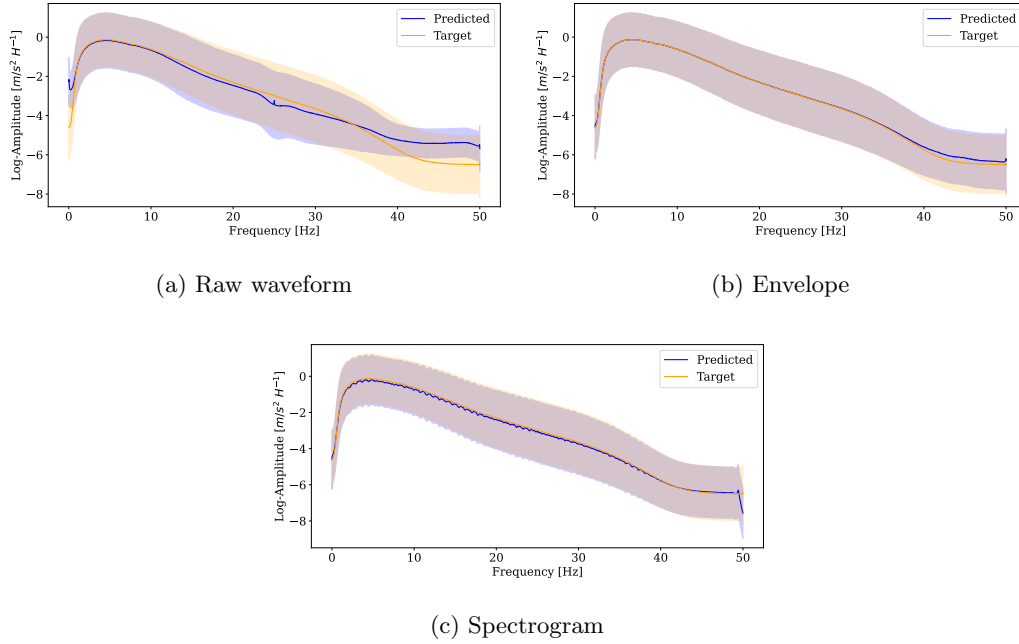


Figure B1: Fourier spectra log-amplitude comparison between the input and output of an autoencoder trained on different representations. The East-West component of the three-channel signal is used for visualization.

Representation	Latent space	Fourier spectra FD ↓			Classifier	
		East-West	North-South	Vertical	Accuracy (%) ↑	Embedding FD ↓
Envelope	✗	2288.64	2246.33	2185.99	8.39	320.90
Envelope	✓	187.95	192.35	190.28	8.33	491.98
Spectrogram	✗	828.41	780.76	867.67	45.82	12.38
Spectrogram	✓	60.98	47.84	56.73	44.48	5.51

Table B1: Ablation study comparing the performance of the diffusion model when trained on the moving average envelope and the spectrogram representation. Results are shown for both direct training on representations and training on the latent space of an autoencoder. The Fréchet Distance (FD) for the log-amplitude Fourier spectra and classifier embeddings is reported between the full data distribution and the generated samples. Classifier accuracy is reported for the generated samples.

Open Research Section

The three-component strong-motion data from the Kiban-Kyoshin (KiK-net) network time series waveforms are provided by the National Research Institute for Earth Science and Disaster Prevention of Japan and can be downloaded at <https://www.bosai.go.jp/e/index.html>. Preprocessed data that was used to train the model is available upon request owing to K-Net and KiK-net dataset policy.

The code for our generative waveform model is available on GitHub at <https://github.com/highfem/tqdne/tags> (Bergmeister et al., 2024). All online pages were last accessed on October 16th, 2024. The supplementary material provides additional information and figures to complement the main content of the primary text, offering a deeper understanding and further validation of the presented results.

Declaration of Competing Interest

The authors declare that there are no conflicts of interest.

Acknowledgments

This work was supported by grant number C22-10 (HighFEM) of the Swiss Data Science Center (SDSC), Ecole Polytechnique Fédérale de Lausanne and ETH Zürich awarded to M.-A. Meier, L. Ermert and M. Koroni. L. Ermert is supported by Swiss National Science Foundation grant 209941. M. Koroni is supported by the Swiss Federal Nuclear Safety Inspectorate (ENSI) under contract number CTR00830. We thank Donat Fäh and Paolo Bergamo for useful discussions on ground motion models and earthquake engineering. We thank CSCS Swiss National Computing Center (Piz Daint under projects sd28 and s1165) and Swiss Seismological Service “Bigstar” Cluster for providing computational resources for this research.

References

- Applied Technology Council. (2009). *Quantification of building seismic performance factors*. US Department of Homeland Security, FEMA.
- Aquib, A. T., & Mai, P. M. (2024, 09). Broadband Ground-Motion Simulations with Machine-Learning-Based High-Frequency Waves from Fourier Neural Operators. *Bulletin of the Seismological Society of America*.
- Arias, A. (1970). A measure of earthquake intensity. *Seismic design for nuclear plants*, 438–483.
- Baker, J., & Allin Cornell, C. (2006). Spectral shape, epsilon and record selection. *Earthquake Engineering & Structural Dynamics*, 35(9), 1077–1095.
- Baker, J., & Bradley, B. (2017). Intensity measure correlations observed in the nga-west2 database, and dependence of correlations on rupture and site parameters. *Earthquake Spectra*, 33(1), 145–156.
- Baker, J., Bradley, B., & Stafford, P. (2021). *Seismic hazard and risk analysis*. Cambridge University Press.
- Bayless, J., & Abrahamson, N. A. (2019). An empirical model for the interfrequency correlation of epsilon for Fourier amplitude spectra. *Bulletin of the Seismological Society of America*, 109(3), 1058–1070.
- Bergamo, P., Hammer, C., & Fäh, D. (2019). *SERA WP7/NA5 - Deliverable 7.4: Towards improvement of site condition indicators* (Report). Zurich: ETH Zurich. doi: 10.3929/ethz-b-000467564
- Bergmeister, A., Palgunadi, K. H., Bosisio, A., Ermert, L., Koroni, M., Perraudin, N., . . . Meier, M.-A. (2024). *Software package “tqdne” for paper titled “High Resolution Seismic Waveform Generation using Denoising Diffusion”*. Zenodo. doi: 10.5281/zenodo.13952381

- Bommer, J., & Acevedo, A. (2004). The use of real earthquake accelerograms as input to dynamic analysis. *Journal of Earthquake Engineering*, 8(spec01), 43–91.
- Boore, D. M. (2003). Simulation of ground motion using the stochastic method. *Pure and applied geophysics*, 160, 635–676.
- Boore, D. M., & Joyner, W. B. (1997). Site amplifications for generic rock sites. *Bulletin of the seismological society of America*, 87(2), 327–341.
- Boore, D. M., Stewart, J. P., Seyhan, E., & Atkinson, G. M. (2014). Nga-west2 equations for predicting pga, pgv, and 5% damped psa for shallow crustal earthquakes. *Earthquake Spectra*, 30(3), 1057–1085.
- Boore, D. M., Watson-Lamprey, J., & Abrahamson, N. A. (2006). Orientation-independent measures of ground motion. *Bulletin of the seismological Society of America*, 96(4A), 1502–1511.
- Chopra, A. K. (2007). *Dynamics of structures*. Pearson Education India.
- Défossez, A., Copet, J., Synnaeve, G., & Adi, Y. (2023). High fidelity neural audio compression. *Transactions on Machine Learning Research*.
- Derras, B., Bard, P.-Y., Cotton, F., & Bekkouche, A. (2012). Adapting the neural network approach to pga prediction: An example based on the kik-net data. *Bulletin of the Seismological Society of America*, 102(4), 1446–1461.
- Dhariwal, P., & Nichol, A. (2021). Diffusion models beat gans on image synthesis. *Advances in neural information processing systems*, 34, 8780–8794.
- Douglas, J. (2003). Earthquake ground motion estimation using strong-motion records: a review of equations for the estimation of peak ground acceleration and response spectral ordinates. *Earth-Science Reviews*, 61(1-2), 43–104.
- Douglas, J., & Aochi, H. (2008). A survey of techniques for predicting earthquake ground motions for engineering purposes. *Surveys in geophysics*, 29, 187–220.
- Esfahani, R. D., Cotton, F., Ohrnberger, M., & Scherbaum, F. (2023). TFCGAN: Nonstationary ground-motion simulation in the time-frequency domain using conditional generative adversarial network (cgan) and phase retrieval methods. *Bulletin of the Seismological Society of America*, 113(1), 453–467.
- Esfahani, R. D., Vogel, K., Cotton, F., Ohrnberger, M., Scherbaum, F., & Kriegerowski, M. (2021). Exploring the dimensionality of ground-motion data by applying autoencoder techniques. *Bulletin of the Seismological Society of America*, 111(3), 1563–1576.
- Florez, M. A., Caporale, M., Buabthong, P., Ross, Z. E., Asimaki, D., & Meier, M.-A. (2022). Data-driven synthesis of broadband earthquake ground motions using artificial intelligence. *Bulletin of the Seismological Society of America*, 112(4), 1979–1996.
- Gatti, F., & Clouteau, D. (2020). Towards blending physics-based numerical simulations and seismic databases using generative adversarial network. *Computer Methods in Applied Mechanics and Engineering*, 372, 113421.
- Goodfellow, I., Pouget-Abadie, J., Mirza, M., Xu, B., Warde-Farley, D., Ozair, S., ... Bengio, Y. (2014). Generative adversarial nets. In *Advances in neural information processing systems*.
- Graves, R., & Pitarka, A. (2010). Broadband ground-motion simulation using a hybrid approach. *Bull Seismol Soc Am*, 100(5A), 2095–2123. doi: 10.1785/0120100057
- Griffin, D., & Lim, J. (1984). Signal estimation from modified short-time Fourier transform. *IEEE Transactions on Acoustics, Speech, and Signal Processing*, 32(2), 236–243.
- Hartzell, S., Harmsen, S., Frankel, A., & Larsen, S. (1999). Calculation of broadband time histories of ground motion: Comparison of methods and validation using strong-ground motion from the 1994 northridge earthquake. *Bulletin of the Seismological Society of America*, 89(6), 1484–1504.
- Heusel, M., Ramsauer, H., Unterthiner, T., Nessler, B., & Hochreiter, S. (2017).

- GANs trained by a two time-scale update rule converge to a local Nash equilibrium. In *Advances in neural information processing systems*.
- Ho, J., Jain, A., & Abbeel, P. (2020). Denoising diffusion probabilistic models. In *Advances in neural information processing systems*.
- Ho, J., Salimans, T., Gritsenko, A., Chan, W., Norouzi, M., & Fleet, D. J. (2022). Video diffusion models. In S. Koyejo, S. Mohamed, A. Agarwal, D. Belgrave, K. Cho, & A. Oh (Eds.), *Advances in neural information processing systems* (Vol. 35, pp. 8633–8646). Curran Associates, Inc.
- Jayalakshmi, S., Dhanya, J., Raghukanth, S., & Mai, P. M. (2021). Hybrid broadband ground motion simulations in the indo-gangetic basin for great himalayan earthquake scenarios. *Bulletin of Earthquake Engineering*, 19, 3319–3348.
- Jozinović, D., Lomax, A., Štajduhar, I., & Michelini, A. (2022). Transfer learning: Improving neural network based prediction of earthquake ground shaking for an area with insufficient training data. *Geophysical Journal International*, 229(1), 704–718.
- Kanno, T., Narita, A., Morikawa, N., Fujiwara, H., & Fukushima, Y. (2006). A new attenuation relation for strong ground motion in japan based on recorded data. *Bulletin of the Seismological Society of America*, 96(3), 879–897.
- Karras, T., Aittala, M., Aila, T., & Laine, S. (2022). Elucidating the design space of diffusion-based generative models. In *Advances in neural information processing systems*.
- Karras, T., Laine, S., & Aila, T. (2019). A style-based generator architecture for generative adversarial networks. In *Proceedings of the ieee/cvf conference on computer vision and pattern recognition* (pp. 4401–4410).
- Karras, T., Laine, S., Aittala, M., Hellsten, J., Lehtinen, J., & Aila, T. (2020). Analyzing and improving the image quality of stylegan. In *Proceedings of the ieee/cvf conference on computer vision and pattern recognition* (pp. 8110–8119).
- Katsanos, E., Sextos, A., & Manolis, G. (2010). Selection of earthquake ground motion records: A state-of-the-art review from a structural engineering perspective. *Soil dynamics and earthquake engineering*, 30(4), 157–169.
- Kingma, D. P., & Welling, M. (2014). Auto-Encoding Variational Bayes. In *International conference on learning representations*.
- Kong, Z., Ping, W., Huang, J., Zhao, K., & Catanzaro, B. (2021). DiffWave: A versatile diffusion model for audio synthesis. In *International conference on learning representations*.
- Li, Y., Ku, B., Zhang, S., Ahn, J.-K., & Ko, H. (2020). Seismic data augmentation based on conditional generative adversarial networks. *Sensors*, 20(23), 6850.
- Li, Z., Meier, M.-A., Hauksson, E., Zhan, Z., & Andrews, J. (2018). Machine learning seismic wave discrimination: Application to earthquake early warning. *Geophysical Research Letters*, 45(10), 4773–4779.
- Lilienkamp, H., von Specht, S., Weatherill, G., Caire, G., & Cotton, F. (2022). Ground-motion modeling as an image processing task: Introducing a neural network based, fully data-driven, and nonergodic approach. *Bulletin of the Seismological Society of America*, 112(3), 1565–1582.
- Luco, N., & Bazzurro, P. (2007). Does amplitude scaling of ground motion records result in biased nonlinear structural drift responses? *Earthquake Engineering & Structural Dynamics*, 36(13), 1813–1835.
- Maechling, P. J., Silva, F., Callaghan, S., & Jordan, T. H. (2015). Seec broadband platform: System architecture and software implementation. *Seismological Research Letters*, 86(1), 27–38.
- Mai, P. M., & Beroza, G. (2002). A spatial random field model to characterize complexity in earthquake slip. *Journal of Geophysical Research: Solid Earth*, 107(B11), ESE–10.
- Mai, P. M., & Beroza, G. (2003). A hybrid method for calculating near-source,

- broadband seismograms: Application to strong motion prediction. *Physics of the Earth and Planetary Interiors*, 137(1-4), 183–199.
- Mai, P. M., Imperatori, W., & Olsen, K. B. (2010). Hybrid broadband ground-motion simulations: Combining long-period deterministic synthetics with high-frequency multiple S-to-S backscattering. *Bull Seismol Soc Am*, 100(5A), 2124–2142. doi: 10.1785/0120080194
- Marano, G. C., Rosso, M. M., Aloisio, A., & Cirrincione, G. (2024). Generative adversarial networks review in earthquake-related engineering fields. *Bulletin of Earthquake Engineering*, 22(7), 3511–3562.
- Matsumoto, Y., Yaoyama, T., Lee, S., Hida, T., & Itoi, T. (2024). Generative Adversarial Networks-Based Ground-Motion Model for Crustal Earthquakes in Japan Considering Detailed Site Conditions. *Bulletin of the Seismological Society of America*.
- Nichol, A. Q., & Dhariwal, P. (2021). Improved denoising diffusion probabilistic models. In *International conference on machine learning* (pp. 8162–8171).
- NIED. (2019). *K-net, kik-net, national research institute for earth science and disaster resilience*. doi: 10.17598/NIED.0004
- Okazaki, T., Hachiya, H., Iwaki, A., Maeda, T., Fujiwara, H., & Ueda, N. (2021). Simulation of broad-band ground motions with consistent long-period and short-period components using the wasserstein interpolation of acceleration envelopes. *Geophysical Journal International*, 227(1), 333–349.
- Olsen, K., & Takedatsu, R. (2015). The sdsu broadband ground-motion generation module bbtoolbox version 1.5. *Seismological Research Letters*, 86(1), 81–88.
- Palgunadi, K. H., Gabriel, A.-A., Garagash, D. I., Ulrich, T., & Mai, P. M. (2024). Rupture dynamics of cascading earthquakes in a multiscale fracture network. *Journal of Geophysical Research: Solid Earth*, 129(3), e2023JB027578.
- Paolucci, R., Gatti, F., Infantino, M., Smerzini, C., Özcebe, A. G., & Stupazzini, M. (2018). Broadband ground motions from 3d physics-based numerical simulations using artificial neural networks. *Bulletin of the Seismological Society of America*, 108(3A), 1272–1286.
- Paolucci, R., Mazzieri, I., Piuanno, G., Smerzini, C., Vanini, M., & Özcebe, A. (2021). Earthquake ground motion modeling of induced seismicity in the Groningen gas field. *Earthquake Engineering & Structural Dynamics*, 50(1), 135–154. Retrieved 2024-10-17, from <https://onlinelibrary.wiley.com/doi/abs/10.1002/eqe.3367> (eprint: <https://onlinelibrary.wiley.com/doi/pdf/10.1002/eqe.3367>) doi: 10.1002/eqe.3367
- Paolucci, R., Smerzini, C., & Vanini, M. (2021, July). BB-SPEEDset: A Validated Dataset of Broadband Near-Source Earthquake Ground Motions from 3D Physics-Based Numerical Simulations. *Bulletin of the Seismological Society of America*, 111(5), 2527–2545. Retrieved 2024-10-15, from <https://doi.org/10.1785/0120210089> doi: 10.1785/0120210089
- Perraudin, N., Balazs, P., & Søndergaard, P. L. (2013). A fast Griffin-Lim algorithm. In *2013 IEEE Workshop on Applications of Signal Processing to Audio and Acoustics* (pp. 1–4).
- Rezende, D., & Mohamed, S. (2015). Variational inference with normalizing flows. In *International conference on machine learning*.
- Rodgers, A. J., Pitarka, A., Pankajakshan, R., Sjögreen, B., & Petersson, N. A. (2020). Regional-scale 3d ground-motion simulations of mw 7 earthquakes on the hayward fault, northern california resolving frequencies 0–10 hz and including site-response corrections. *Bulletin of the Seismological Society of America*, 110(6), 2862–2881.
- Rombach, R., Blattmann, A., Lorenz, D., Esser, P., & Ommer, B. (2022). High-resolution image synthesis with latent diffusion models. In *Proceedings of the IEEE/CVF conference on computer vision and pattern recognition*.

- Saikia, C. K., & Somerville, P. (1997). Simulated hard-rock motions in saint louis, missouri, from large new madrid earthquakes ($m_w \geq 6.5$). *Bulletin of the Seismological Society of America*, 87(1), 123–139.
- Savran, W., & Olsen, K. (2019). Ground motion simulation and validation of the 2008 chino hills earthquake in scattering media. *Geophysical Journal International*, 219(3), 1836–1850.
- Shi, Y., Lavrentiadis, G., Asimaki, D., Ross, Z. E., & Azizzadenesheli, K. (2024). Broadband ground-motion synthesis via generative adversarial neural operators: Development and validation. *Bulletin of the Seismological Society of America*, 114(4), 2151–2171.
- Smerzini, C., Amendola, C., Paolucci, R., & Bazrafshan, A. (2024, February). Engineering validation of BB-SPEEDset, a data set of near-source physics-based simulated accelerograms. *Earthquake Spectra*, 40(1), 420–445. Retrieved 2024-10-15, from <http://journals.sagepub.com/doi/10.1177/87552930231206766> doi: 10.1177/87552930231206766
- Song, Y., & Ermon, S. (2019). Generative modeling by estimating gradients of the data distribution. In *Advances in neural information processing systems*.
- Song, Y., Sohl-Dickstein, J., Kingma, D. P., Kumar, A., Ermon, S., & Poole, B. (2021). Score-based generative modeling through stochastic differential equations. In *International conference on learning representations*.
- Tang, Y., & Mai, P. M. (2023). Stochastic ground-motion simulation of the 2021 m w 5.9 woods point earthquake: Facilitating local probabilistic seismic hazard analysis in australia. *Bulletin of the Seismological Society of America*, 113(5), 2119–2143.
- thispersondoesnotexist.com. (2023). *This person does not exist*. <https://thispersondoesnotexist.com>. (Accessed: 2024-10-16)
- Touhami, S., Gatti, F., Lopez-Caballero, F., Cottreau, R., de Abreu Corrêa, L., Aubry, L., & Clouteau, D. (2022). Sem3d: A 3d high-fidelity numerical earthquake simulator for broadband (0–10 hz) seismic response prediction at a regional scale. *Geosciences*, 12(3), 112.
- van Ede, M. C., Molinari, I., Imperatori, W., Kissling, E., Baron, J., & Morelli, A. (2020). Hybrid broadband seismograms for seismic shaking scenarios: An application to the po plain sedimentary basin (northern italy). *Pure and Applied Geophysics*, 177(5), 2181–2198.
- Vincent, P. (2011). A connection between score matching and denoising autoencoders. *Neural Computation*, 23(7), 1661–1674.
- Wang, T., Trugman, D., & Lin, Y. (2021). Seismogen: Seismic waveform synthesis using gan with application to seismic data augmentation. *Journal of Geophysical Research: Solid Earth*, 126(4), e2020JB020077.
- Woollam, J., Münchmeyer, J., Tilmann, F., Rietbrock, A., Lange, D., Bornstein, T., ... others (2022). Seisbench—a toolbox for machine learning in seismology. *Seismological Society of America*, 93(3), 1695–1709.

Supporting Information for "High Resolution Seismic Waveform Generation using Denoising Diffusion"

The content of the supplementary figures is listed as follows:

1. Figures S1 to S42

Introduction

This supplementary material provides additional information and figures to complement the main content of the primary text. The aim is to offer a deeper understanding and further validate the presented results. This document includes visual representations that support and enhance the findings discussed in the main text.

Additional figures for evaluation metrics for the generative waveform model (GWM) and the real data for different bins of magnitudes, hypocentral distances, faulting type, and V_{S30} :

1. Time domain signal envelopes.
2. Fourier spectral amplitude.
3. Shaking duration statistic for all magnitudes
4. Pseudo-spectral acceleration for period $T = 0.1, 0.3$ and 1.0 s versus distances.
5. Pseudo-spectral acceleration versus magnitudes.
6. Pseudo-spectral acceleration versus V_{S30} .
7. Average model probabilities across magnitude and distance bin.
8. Residual of spectral mean amplitude.

Figures:

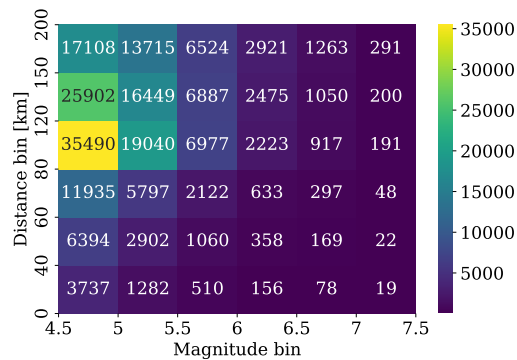


Figure S1: Number of samples in each magnitude-distance bin for all of the following bin plots. Predicted and target denote the generative waveform model (GWM) and real data.

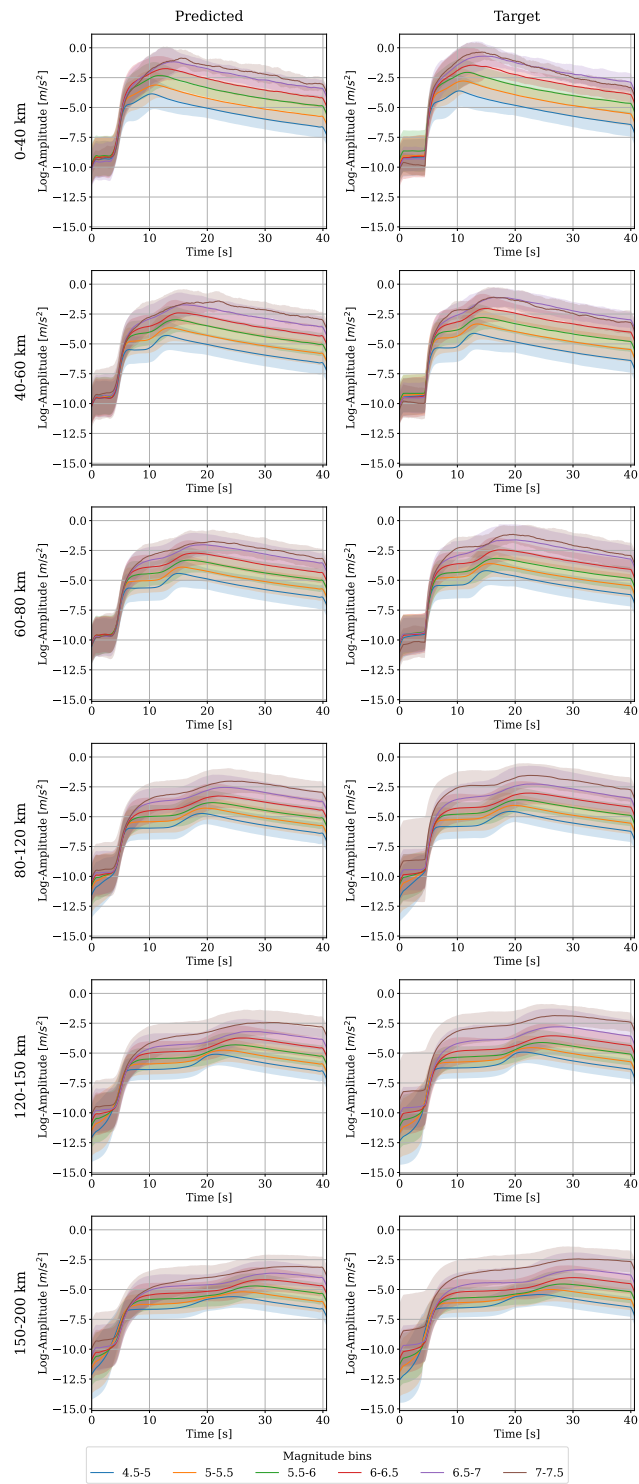


Figure S2: Distribution of time-domain envelopes for East-West-component seismograms in different magnitude and distance bins. Predicted and target denote the generative waveform model (GWM) and real data.

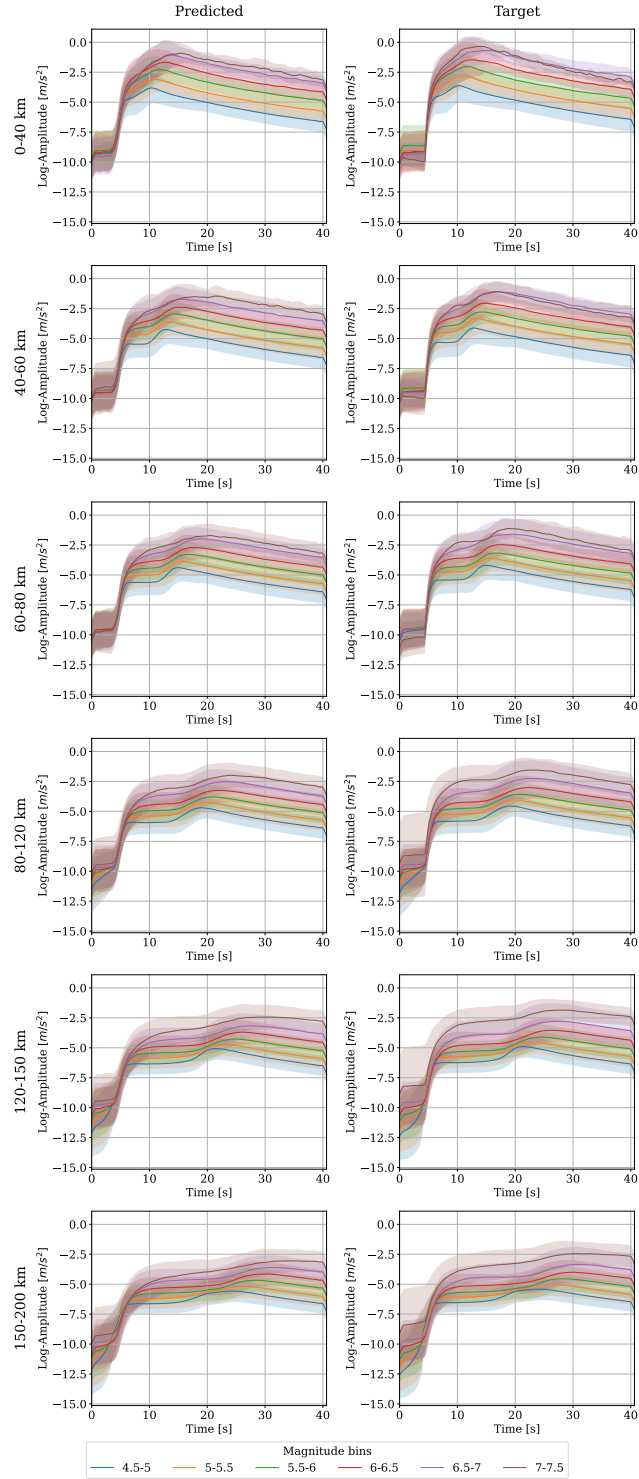


Figure S3: Distribution of time-domain envelopes for North-South-component seismograms in different magnitude and distance bins. Predicted and target denote the generative waveform model (GWM) and real data.

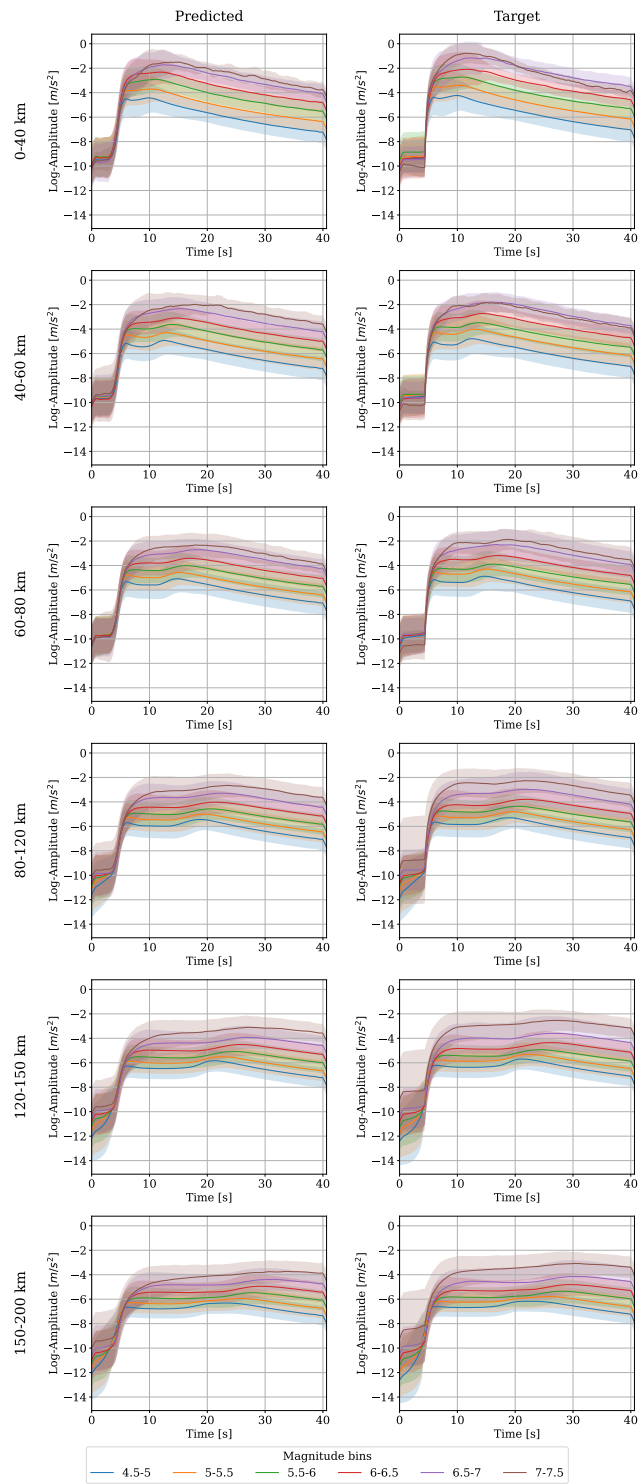


Figure S4: Distribution of time-domain envelopes for vertical-component seismograms in different magnitude and distance bins. Predicted and target denote the generative waveform model (GWM) and real data.

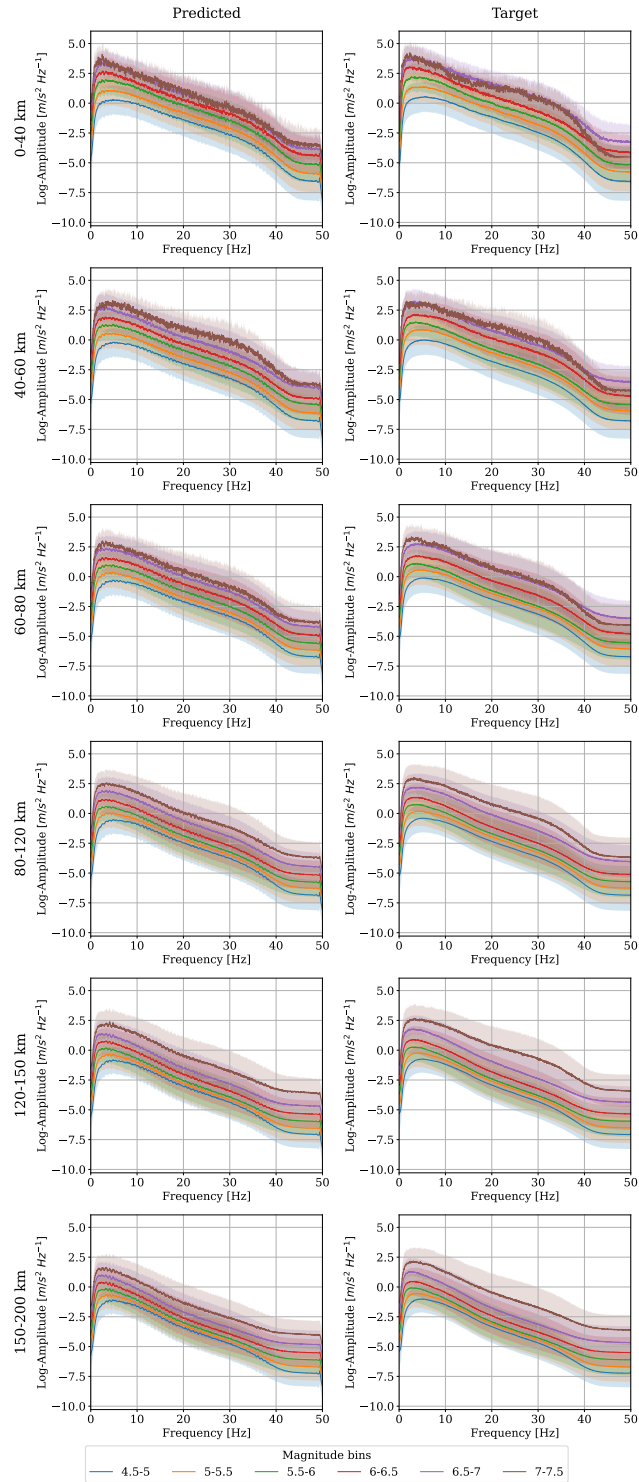


Figure S5: Distribution of Fourier spectra log-amplitudes for East-West-component seismograms in different magnitude and distance bins. Predicted and target denote the generative waveform model (GWM) and real data.

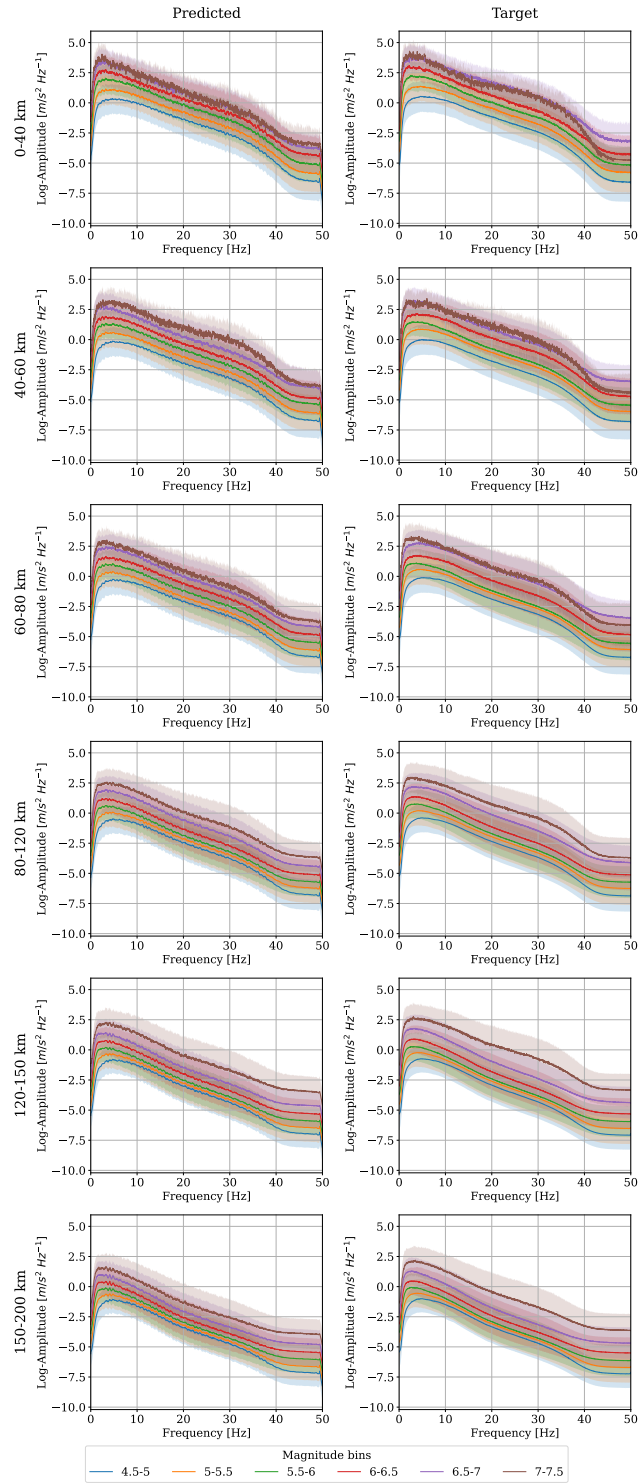


Figure S6: Distribution of Fourier spectra log-amplitudes for North-South-component seismograms in different magnitude and distance bins. Predicted and target denote the generative waveform model (GWM) and real data.

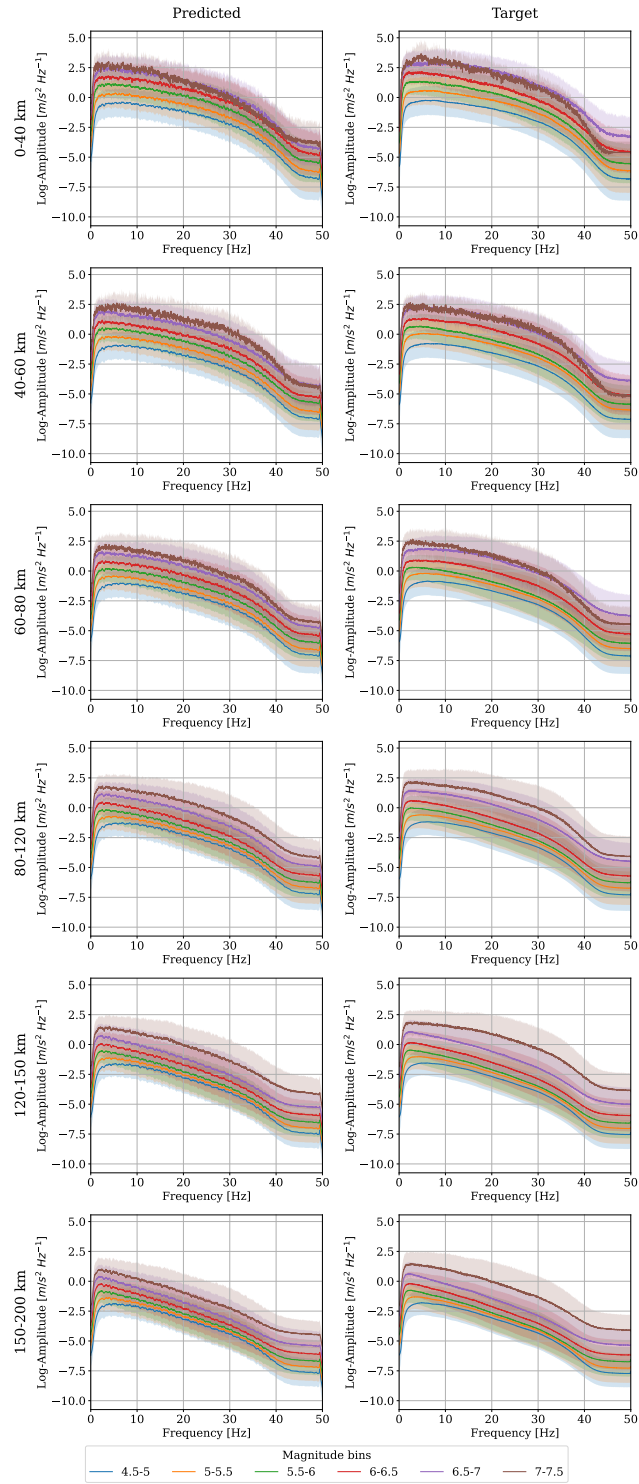


Figure S7: Distribution of Fourier spectra log-amplitudes for vertical-component seismograms in different magnitude and distance bins. Predicted and target denote the generative waveform model (GWM) and real data.

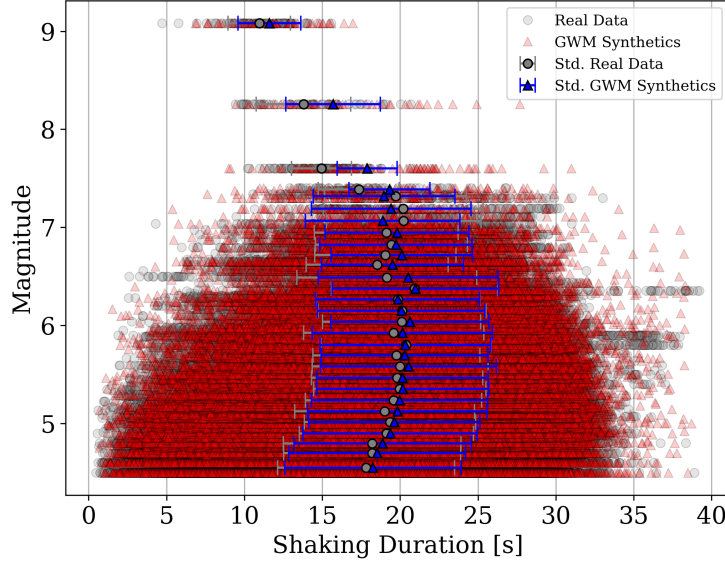


Figure S8: Shaking duration for all GWM synthetics (red triangles) using one realization and real data (grey circles) with corresponding conditioning parameters. For each magnitude bin (every 0.08) from M 4.5 - 9.0, grey dots and lines show the mean and standard deviation of the real data, while blue triangles and lines show the mean and standard deviation of the GWM synthetics.

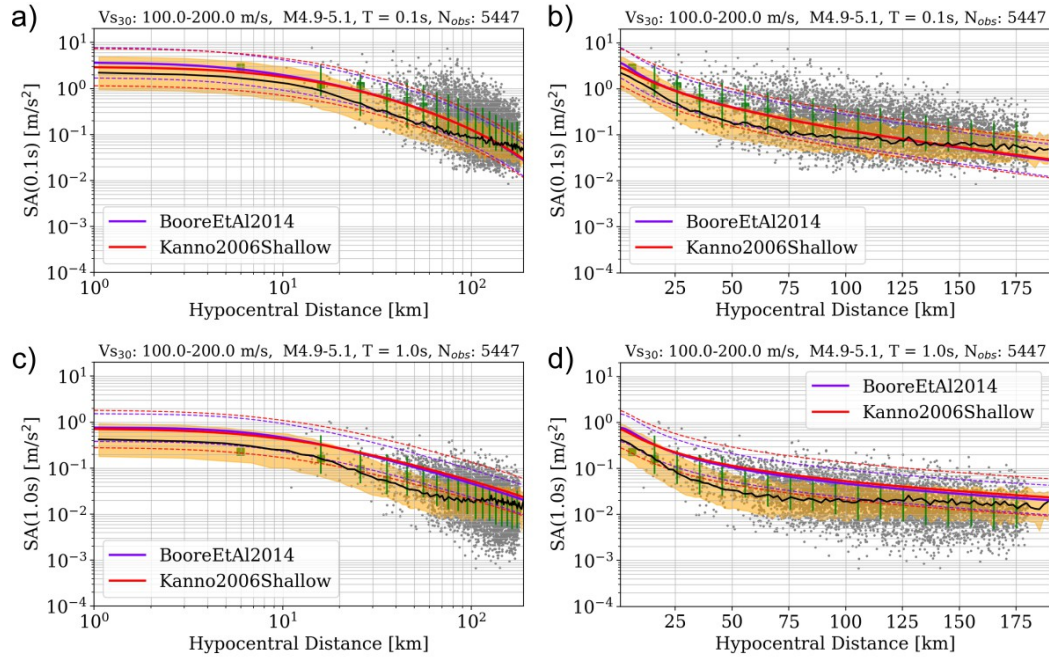


Figure S9: RotD50 pseudo-spectral acceleration (SA) with a damping factor 5% versus hypocentral distance for periods (T) of 0.1 s and 1.0 s. Median prediction of the GWM (black line) and standard deviation (yellow shaded area), along with median prediction (solid lines) and standard deviation (dashed lines) of the Boore et al. (2014) GMM (violet), and the Kanno et al. (2006) GMM (red), using $M5$ and $V_{S30} = 150$ m/s. The data are sampled from narrow magnitude and V_{S30} bins, as written in the figure titles, and shown by their median (green squares) and standard deviations (green lines).

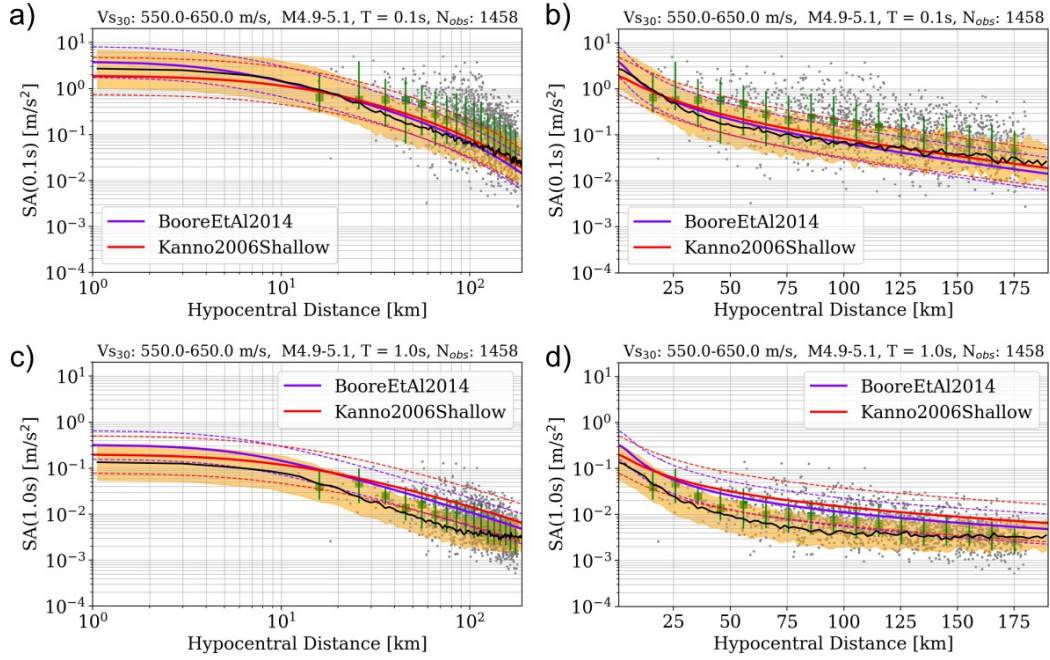


Figure S10: Same as Figure S9 but for the magnitude bin M5 and $V_{S30} = 600$ m/s.

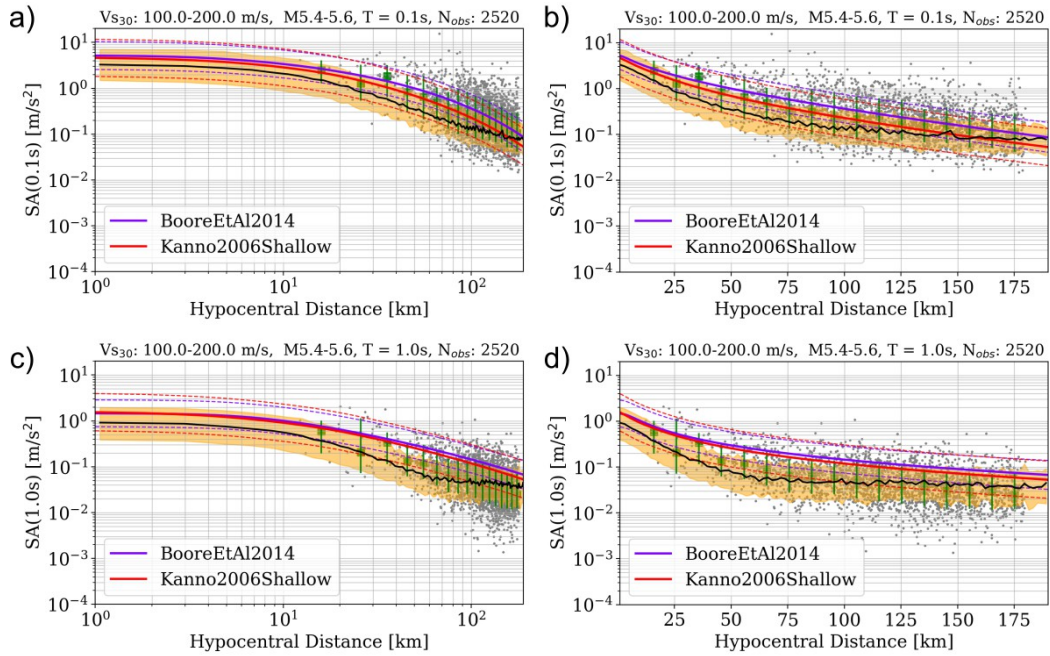


Figure S11: Same as Figure S9 but for the magnitude bin M5.5 and $V_{S30} = 150$ m/s.

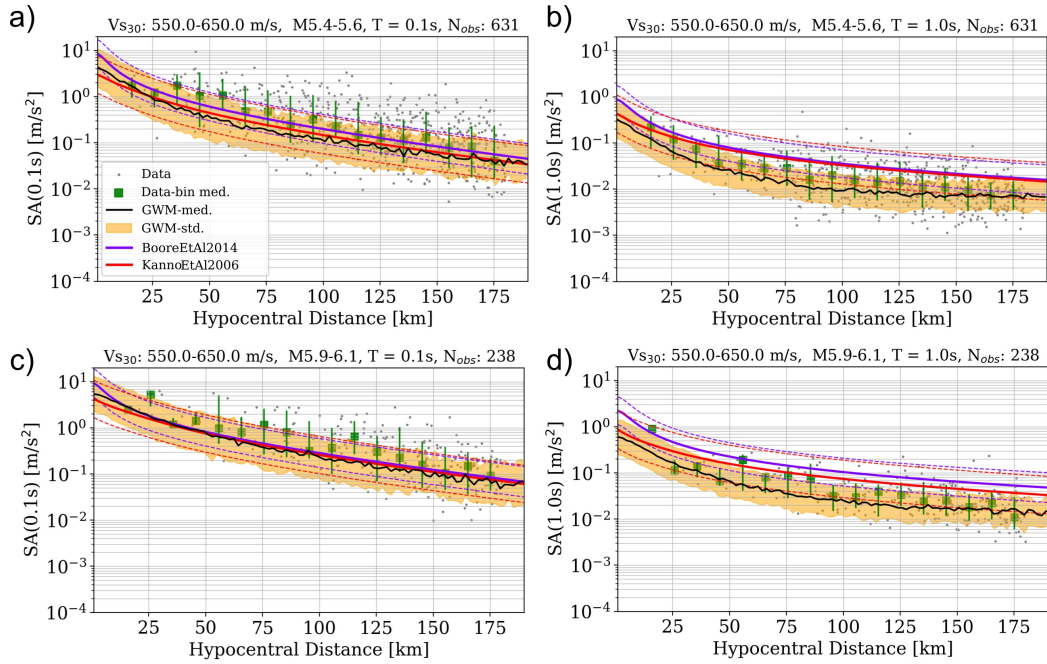


Figure S12: Same as Figure S9 but for the magnitude bin M5.5 and $V_{S30} = 600$ m/s.

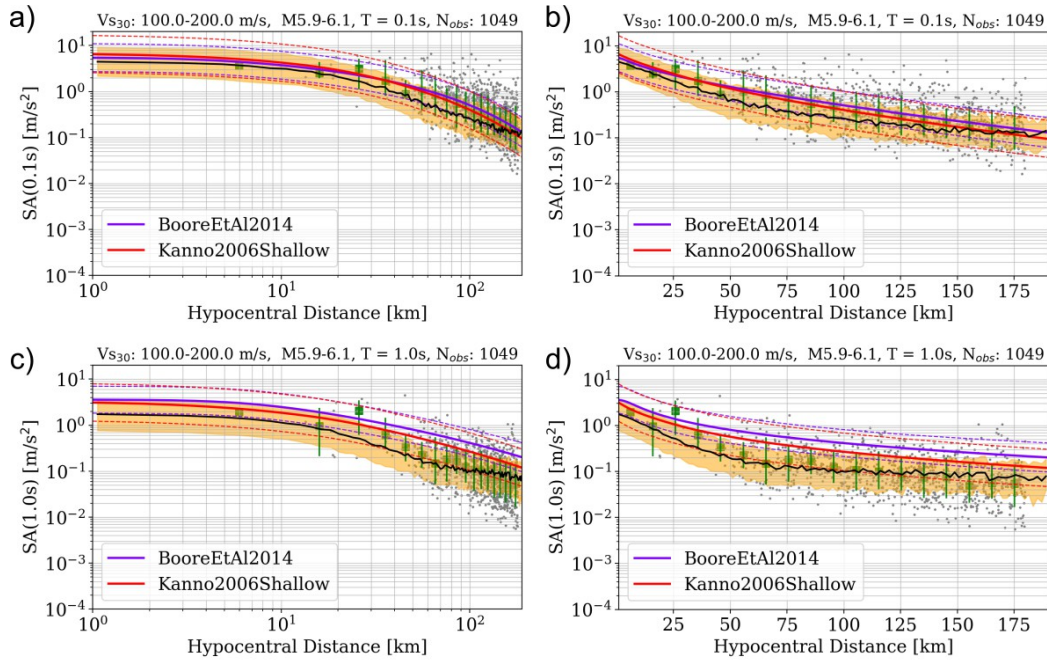


Figure S13: Same as Figure S9 but for the magnitude bin M6.0 and $V_{S30} = 150$ m/s.

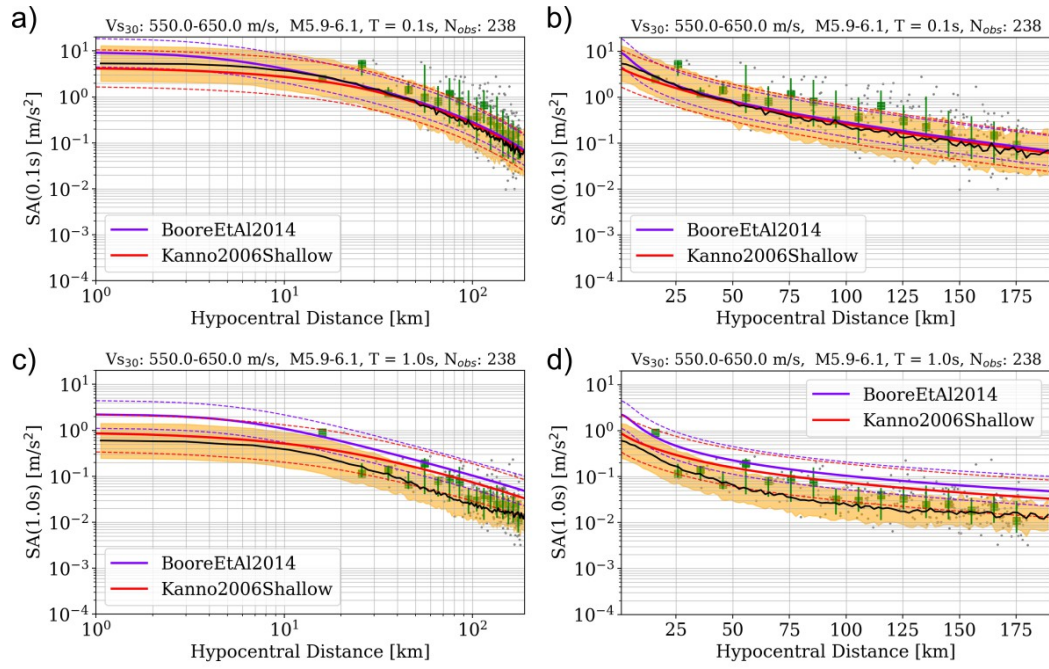


Figure S14: Same as Figure S9 but for the magnitude bin $M6.0$ and $V_{S30} = 600$ m/s.

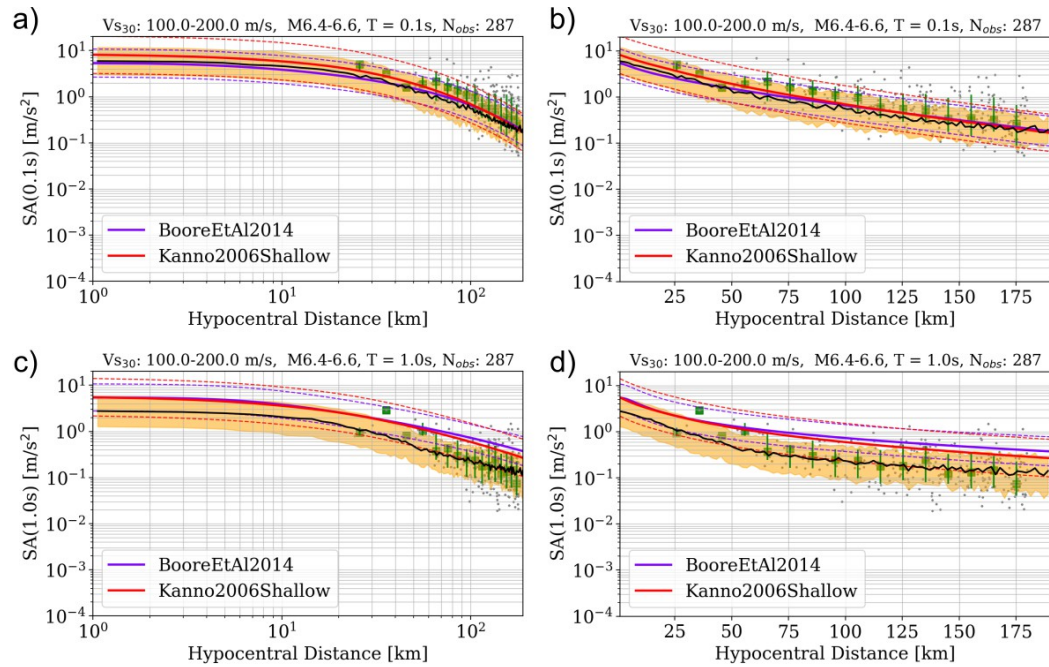


Figure S15: Same as Figure S9 but for the magnitude bin $M6.5$ and $V_{S30} = 150$ m/s.

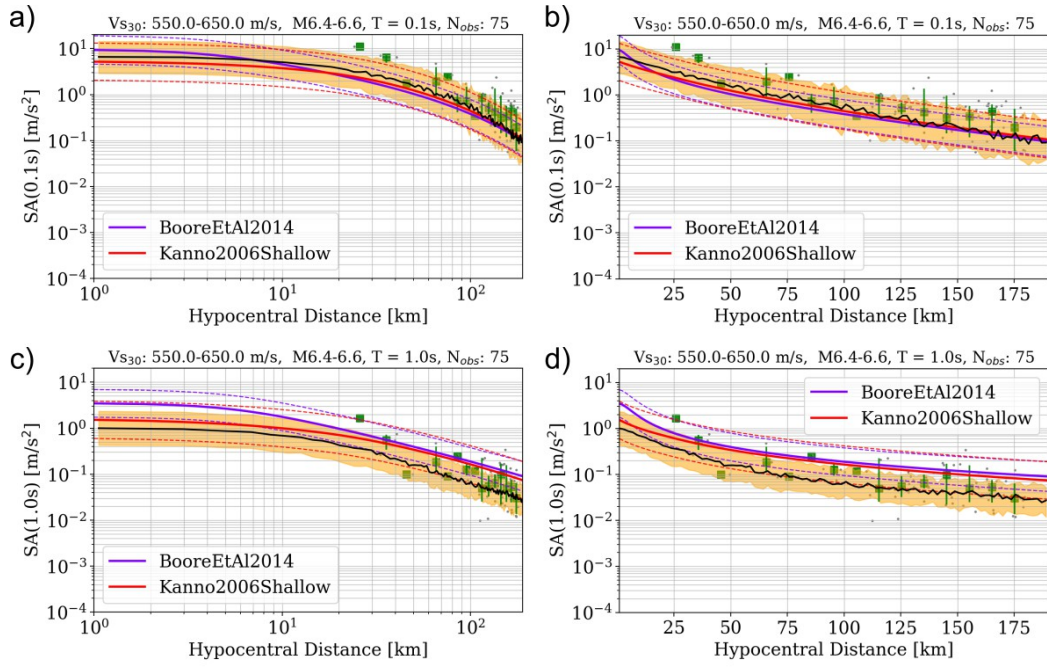


Figure S16: Same as Figure S9 but for the magnitude bin M6.5 and $V_{S30} = 600$ m/s.

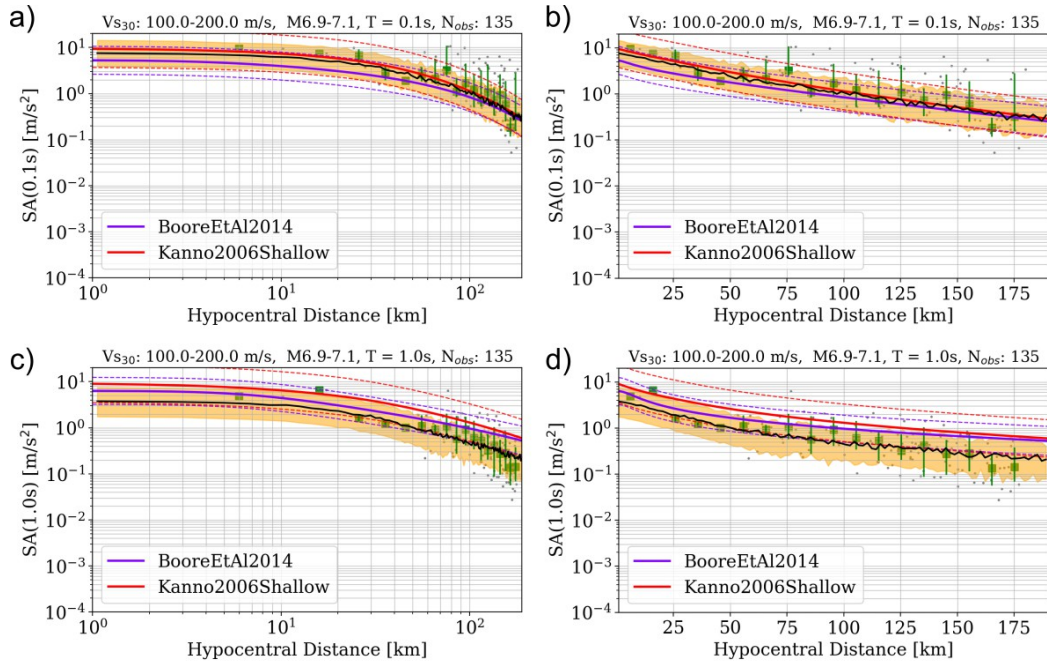


Figure S17: Same as Figure S9 but for the magnitude bin M7.0 and $V_{S30} = 150$ m/s.

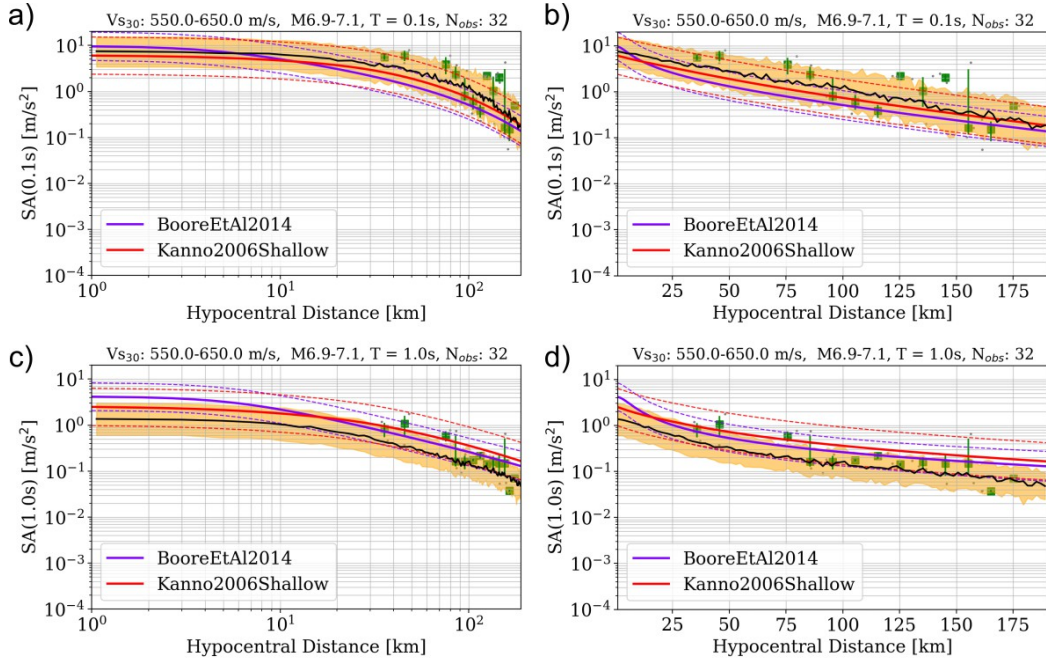


Figure S18: Same as Figure S9 but for the magnitude bin M7.0 and $V_{S30} = 600$ m/s.

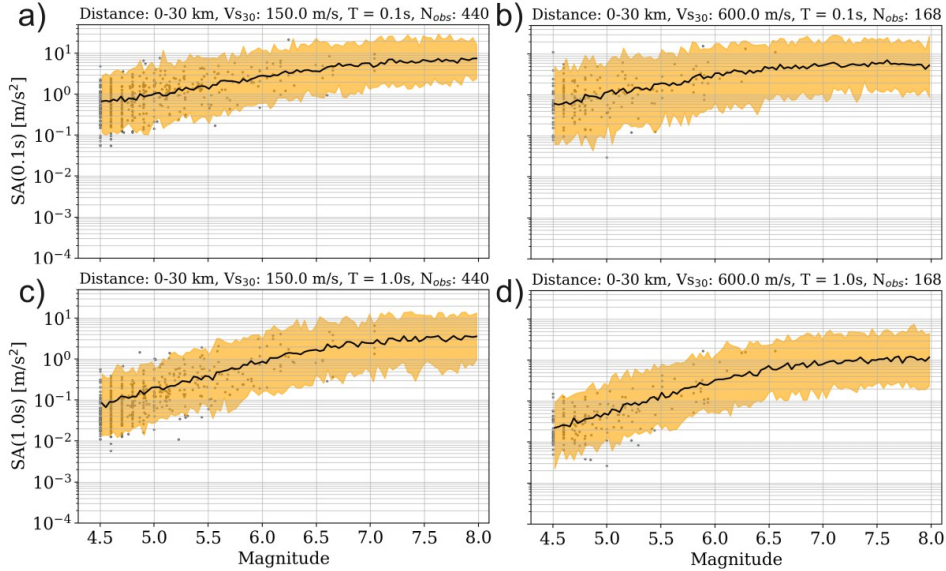


Figure S19: RotD50 pseudo-spectral acceleration (SA) with a damping factor of 5% versus magnitude. Median of the GWM prediction (black lines) and its standard deviation (yellow shaded areas), using $R = 15$ km. Panels a) and c) show RotD50 pseudo-spectral acceleration for $V_{S30} = 150$ m/s at periods of 0.1 s and 1.0 s, respectively. Panels b) and d) show RotD50 pseudo-spectral acceleration for $V_{S30} = 600$ m/s at periods of 0.1 s and 1.0 s, respectively. The data (grey dots) are sampled from narrow magnitude, R , and V_{S30} bins, as written in the figure titles.

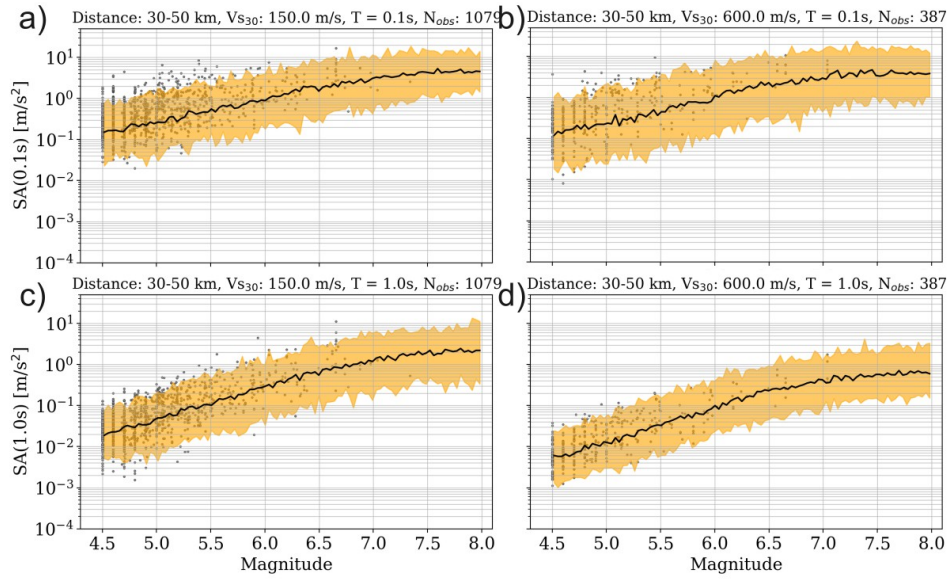


Figure S20: Same as Figure S19 a distance bin of 40 km.

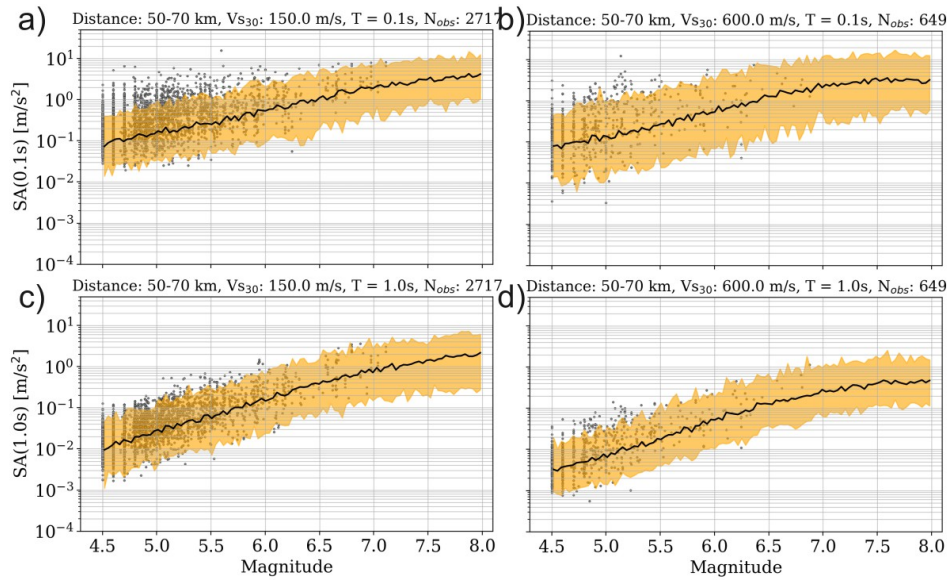


Figure S21: Same as Figure S19 a distance bin of 60 km.

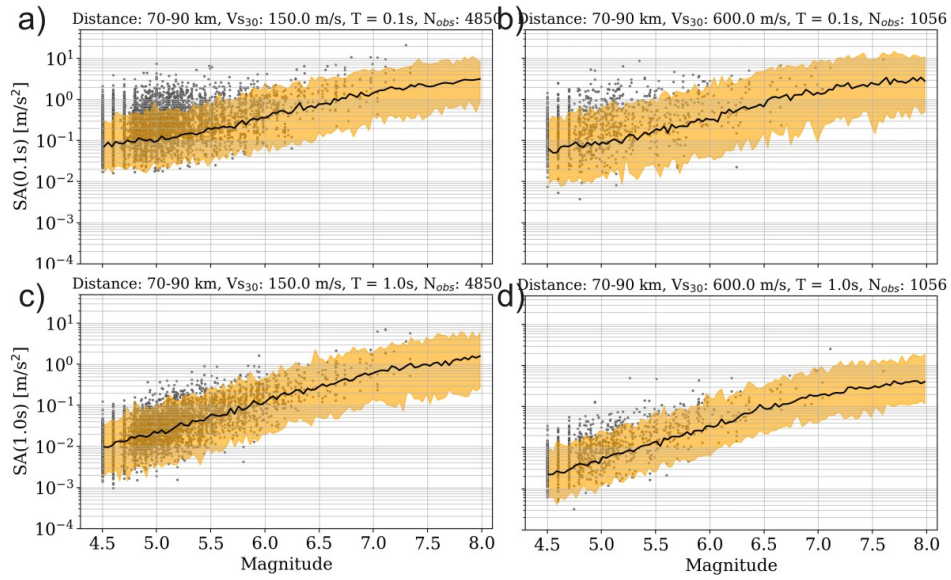


Figure S22: Same as Figure S19 a distance bin of 80 km.

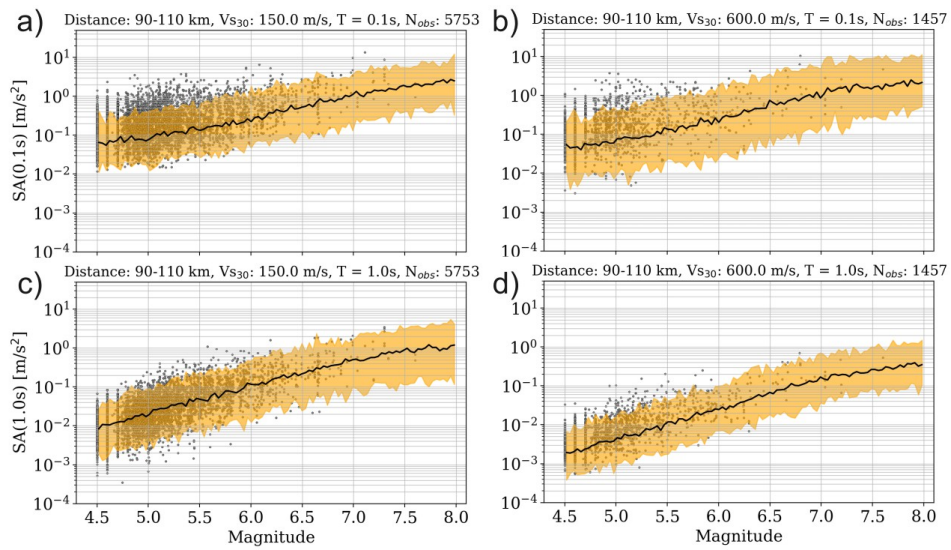


Figure S23: Same as Figure S19 a distance bin of 100 km.

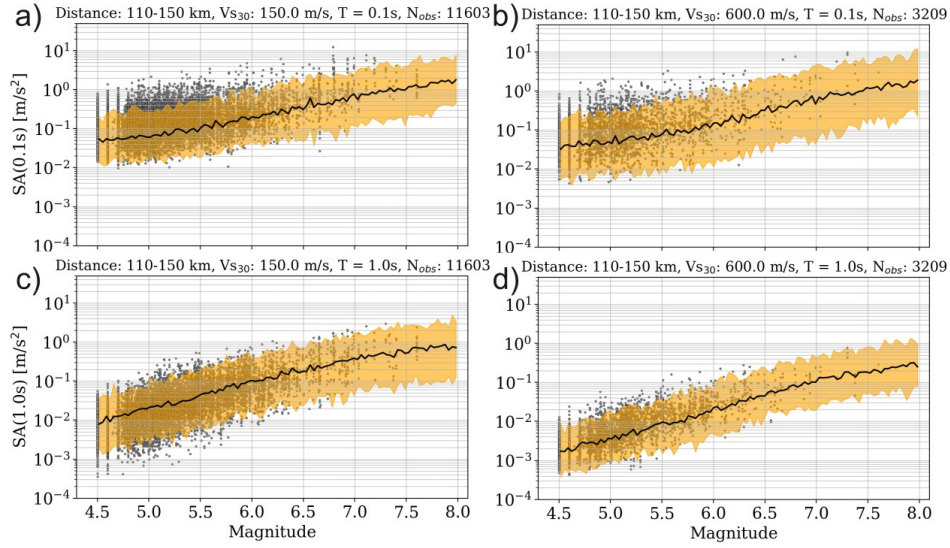


Figure S24: Same as Figure S19 a distance bin of 130 km.

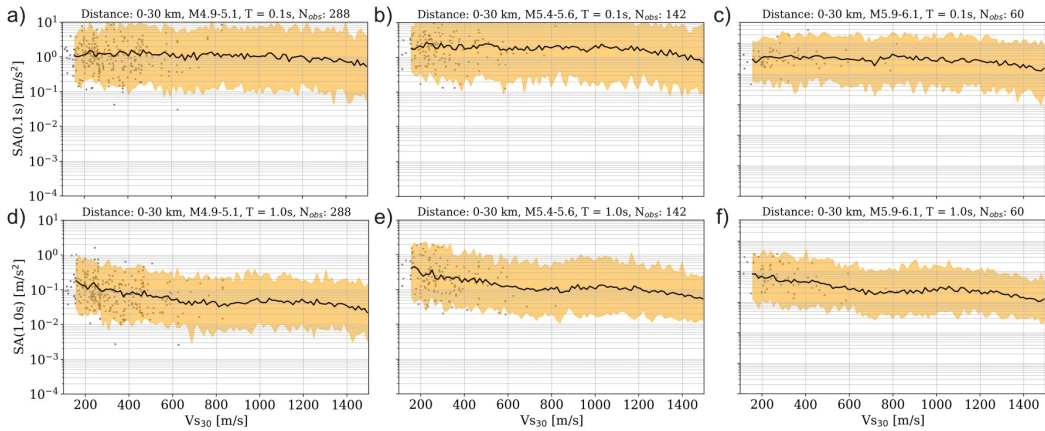


Figure S25: RotD50 pseudo-spectral acceleration (SA) with a damping factor of 5% versus magnitude. Median of the GWM prediction (black lines) and its standard deviation (yellow shaded areas), using $R = 15$ km. Panels a) and d) show RotD50 pseudo-spectral acceleration for $M5$ m/s at periods of 0.1 s and 1.0 s, respectively. Panels b) and e) show RotD50 pseudo-spectral acceleration for $M5.5$ m/s at periods of 0.1 s and 1.0 s, respectively. Panels c) and f) show RotD50 pseudo-spectral acceleration for $M6.0$ m/s at periods of 0.1 s and 1.0 s, respectively. The data (grey dots) are sampled from narrow magnitude, R , and magnitude bins, as written in the figure titles.

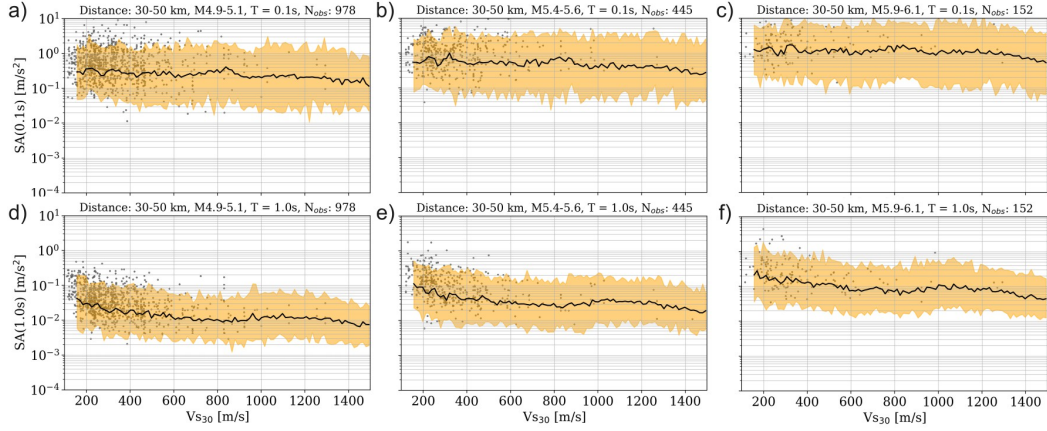


Figure S26: Same as Figure S25 but with a distance bin of 40 km.

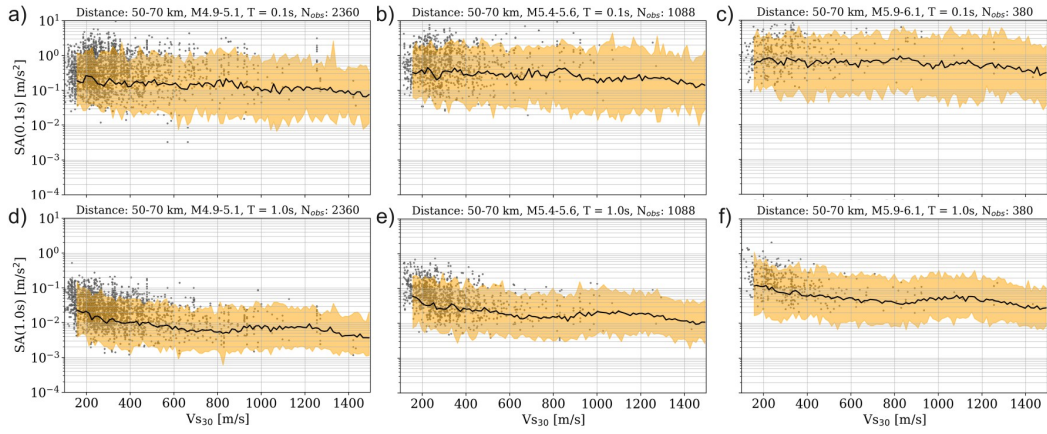


Figure S27: Same as Figure S25 but with a distance bin of 60 km.

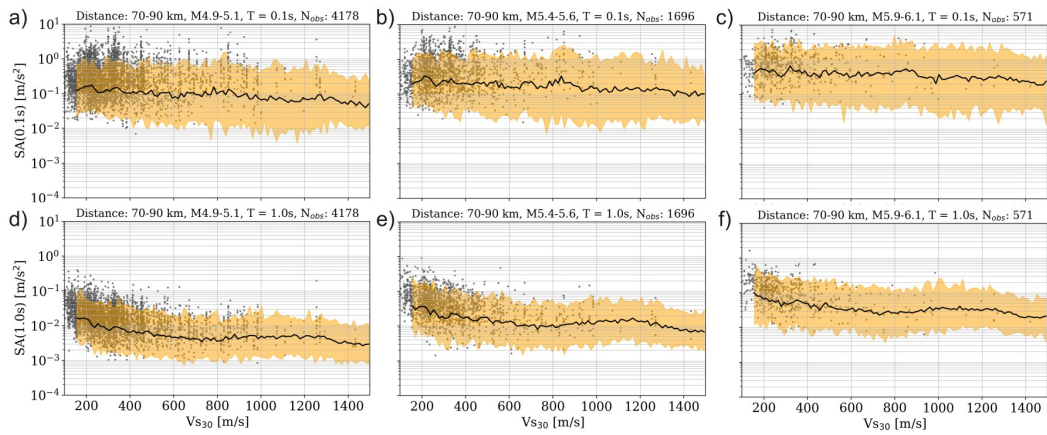


Figure S28: Same as Figure S25 but with a distance bin of 80 km.

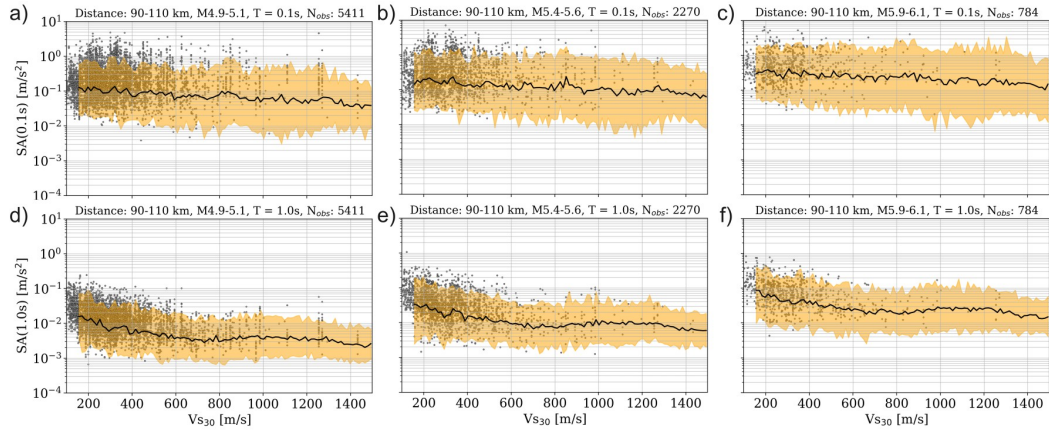


Figure S29: Same as Figure S25 but with a distance bin of 100 km.

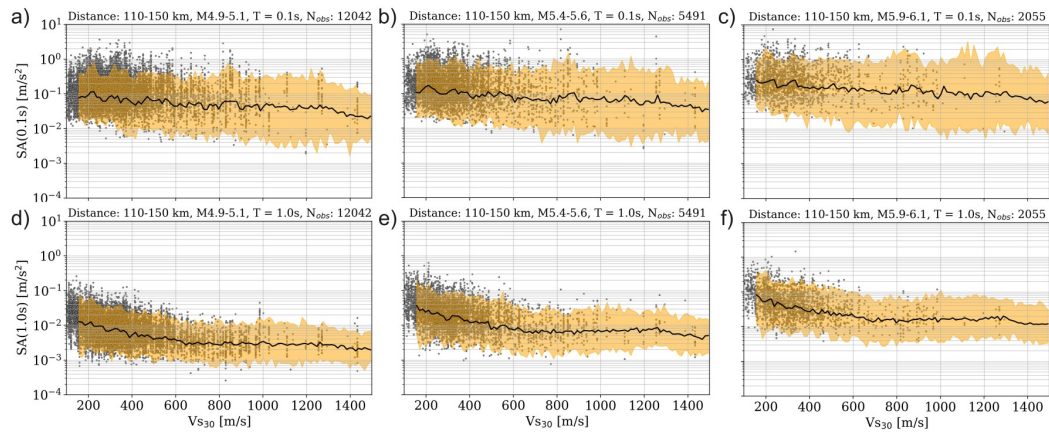


Figure S30: Same as Figure S25 but with a distance bin of 130 km.

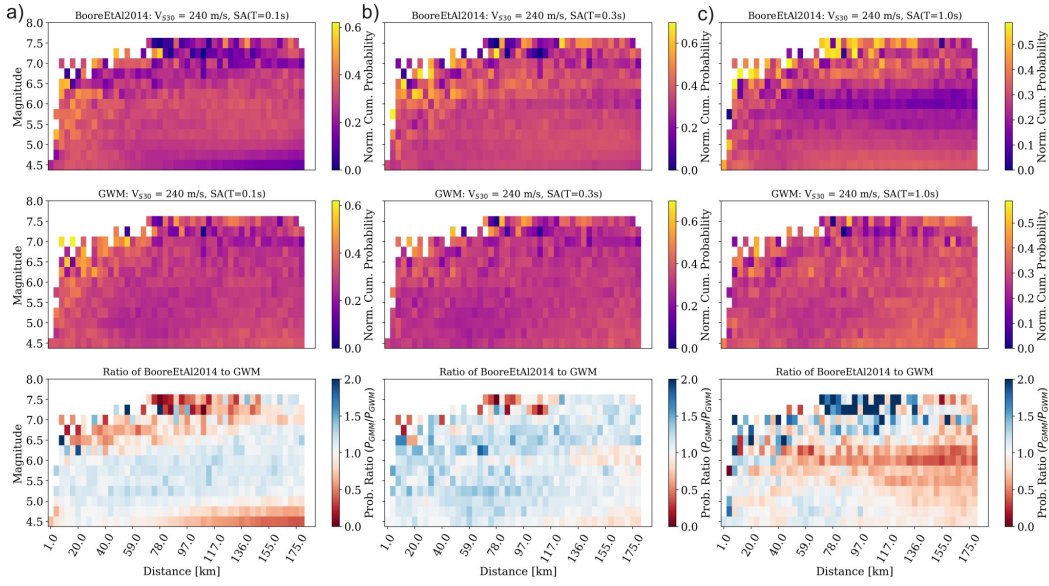


Figure S31: Average model probabilities given the SA data of the ground motion model (GMM) by (Boore et al., 2014), generative waveform modeling (GWM), and the ratio between the two distributions given the data as a function of magnitude and recording distance for $V_{S30} = 240$ m/s. Panels a), b), and c) show the model likelihoods and their ratios at $T = 0.1$ s, $T = 0.3$ s, and $T = 1.0$ s, respectively.

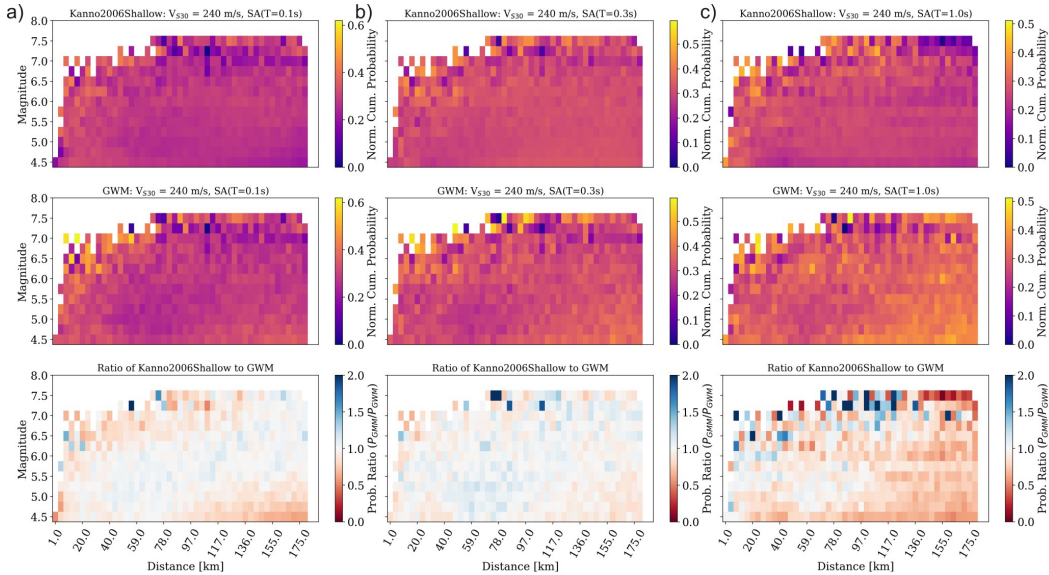


Figure S32: Same as Figure S31 but for GMM model of (Kanno et al., 2006) for $V_{S30} = 240$ m/s. Panels a), b), and c) show the model likelihoods and their ratios at $T = 0.1$ s, $T = 0.3$ s, and $T = 1.0$ s, respectively.

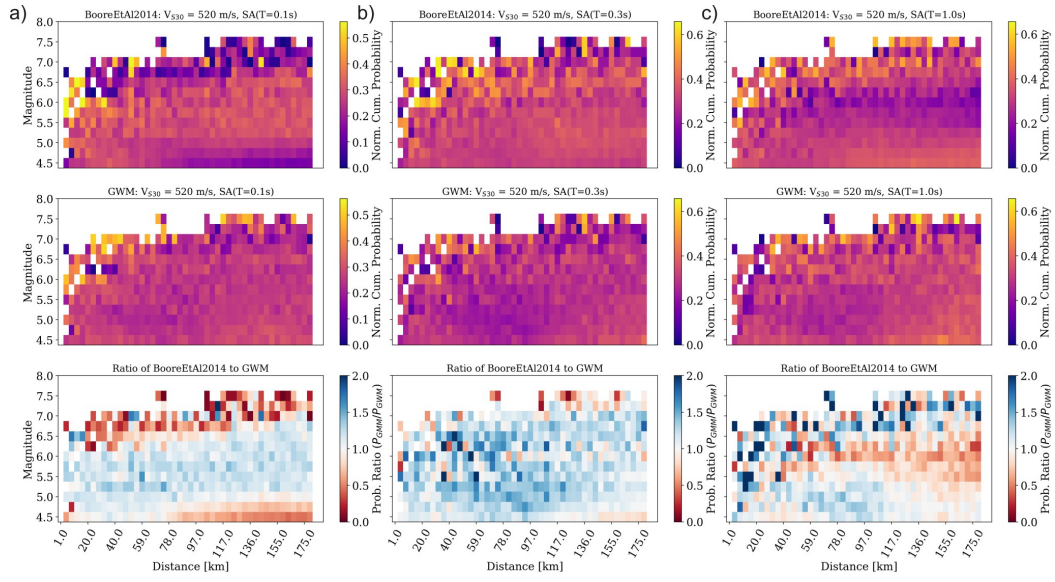


Figure S33: Same as Figure S31 but for $V_{S30} = 520$ m/s.

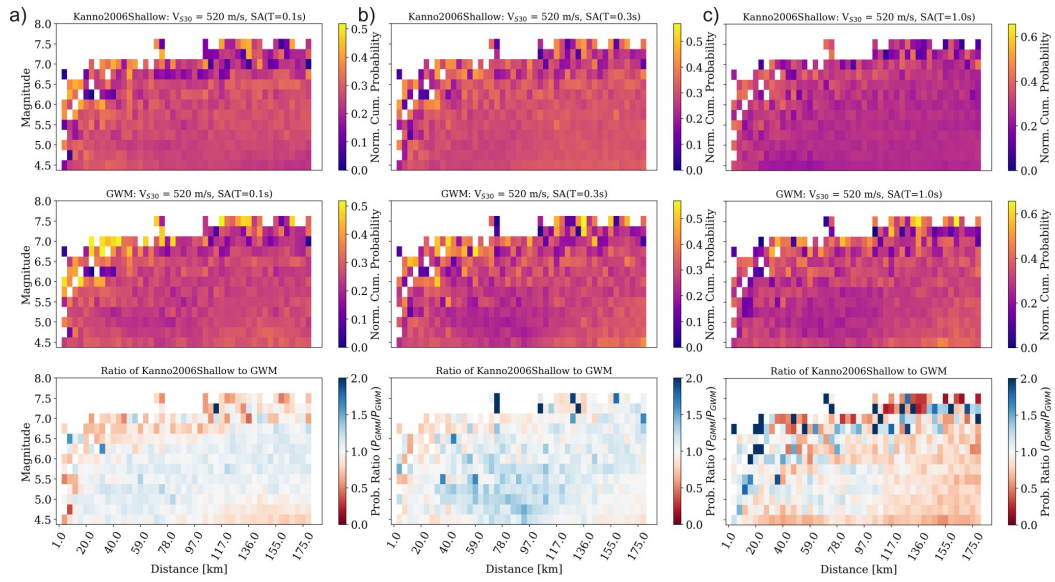


Figure S34: Same as Figure S32 but for $V_{S30} = 520$ m/s.

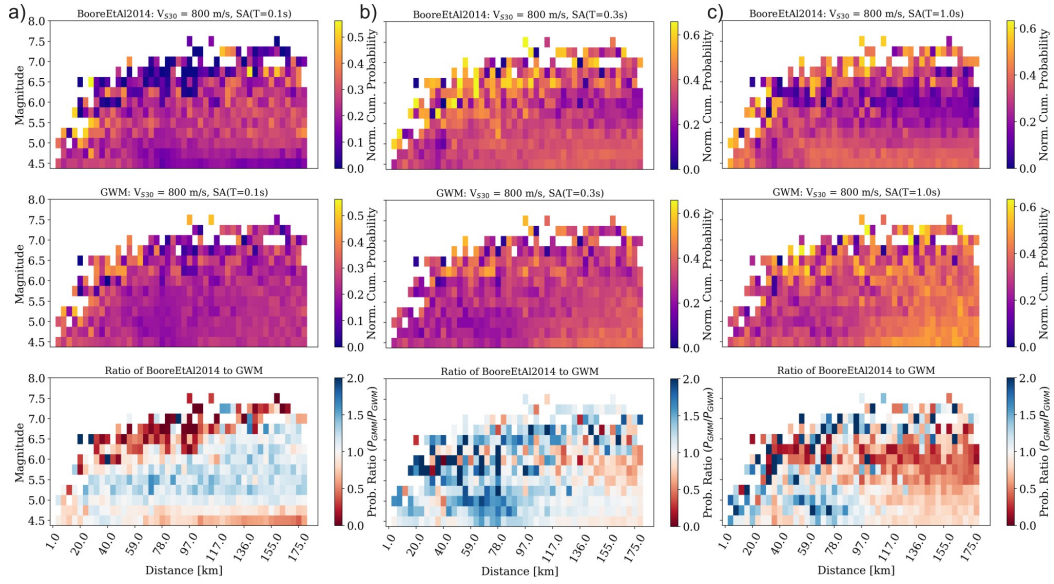


Figure S35: Same as Figure S31 but for $V_{S30} = 800$ m/s.

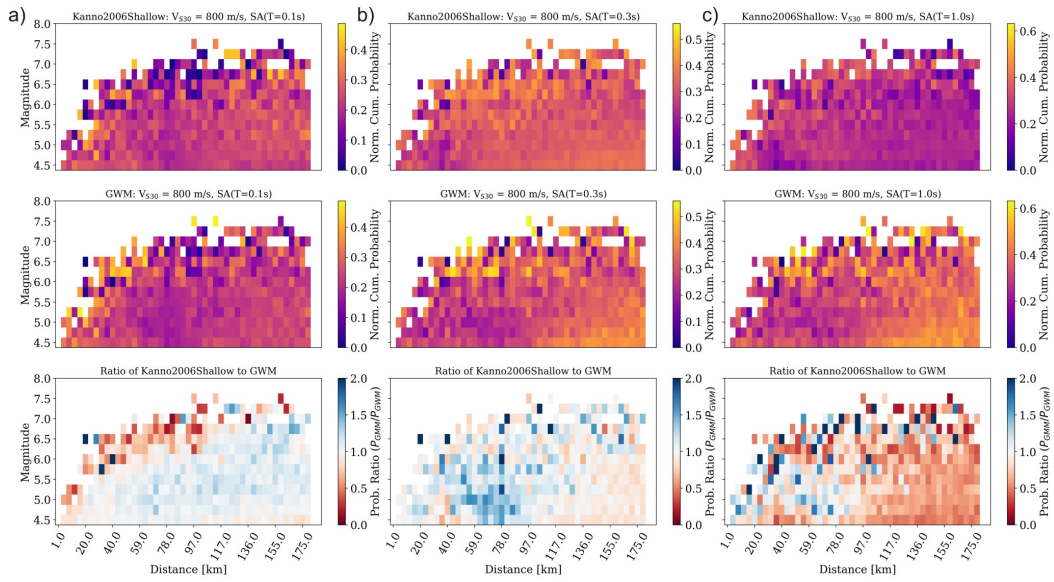


Figure S36: Same as Figure S32 but for $V_{S30} = 800$ m/s.

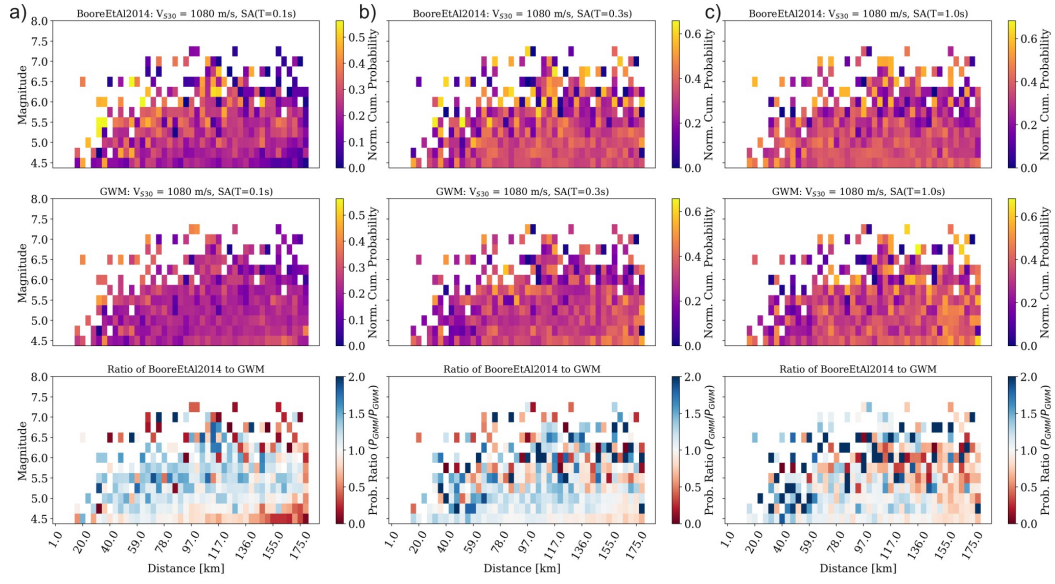


Figure S37: Same as Figure S31 but for $V_{S30} = 1080$ m/s.

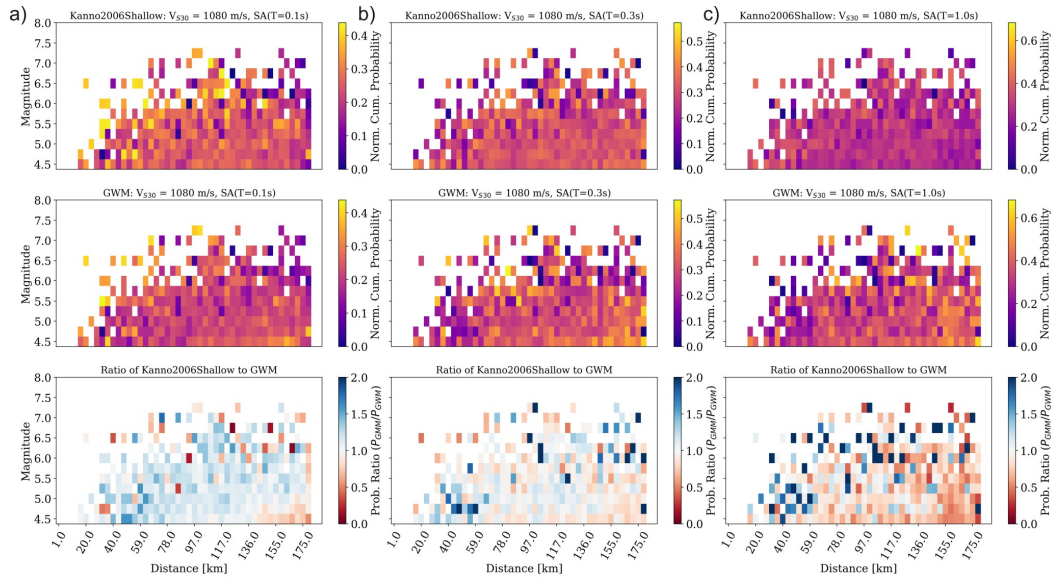


Figure S38: Same as Figure S32 but for $V_{S30} = 1080$ m/s.

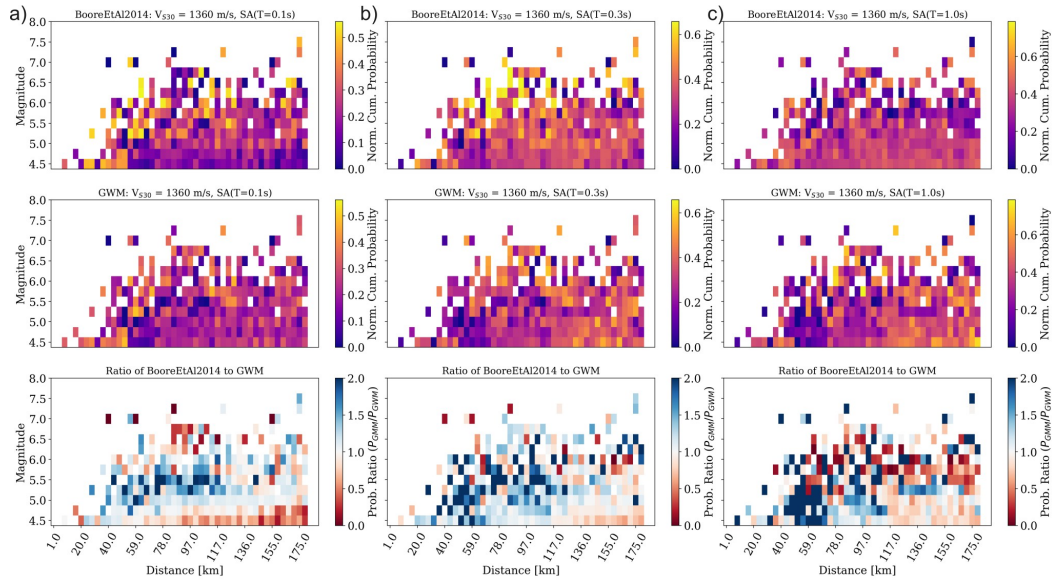


Figure S39: Same as Figure S31 but for $V_{S30} = 1360$ m/s.

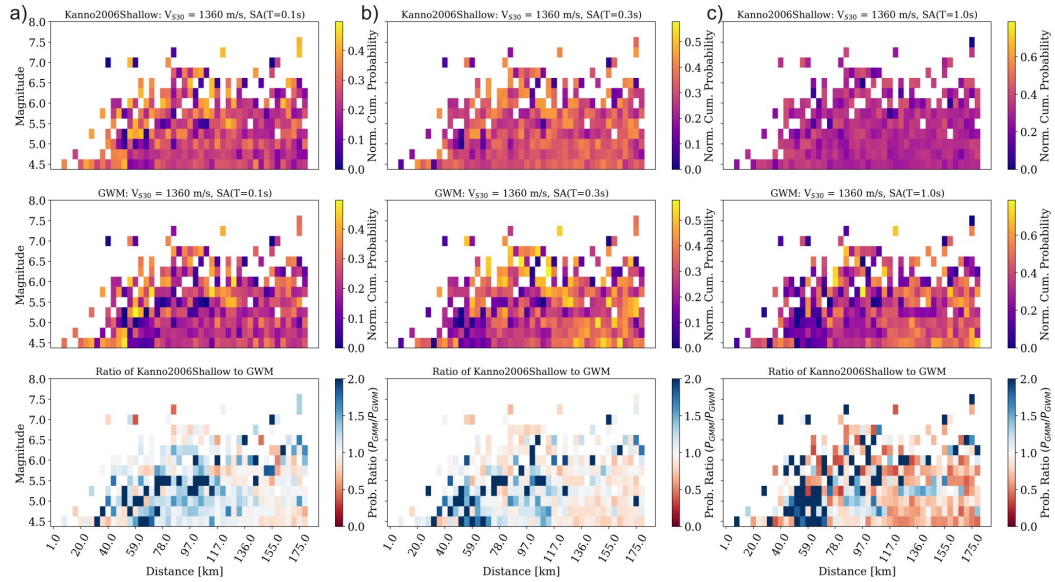


Figure S40: Same as Figure S32 but for $V_{S30} = 1360$ m/s.

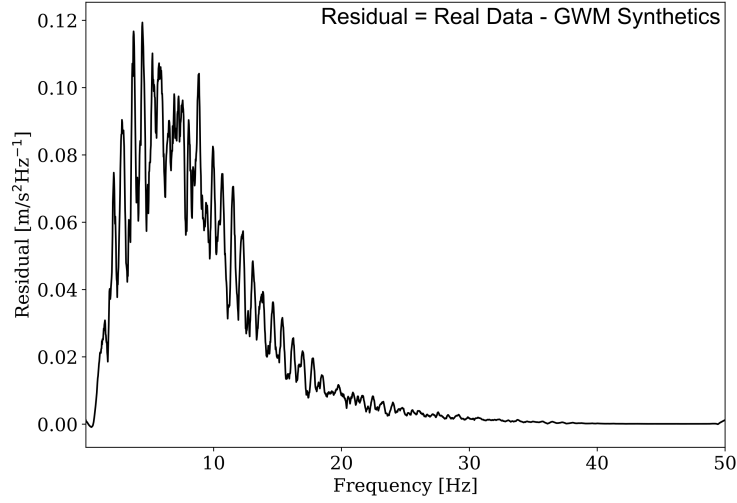


Figure S41: Residual of the spectral mean amplitude between real data and GWM for all records.

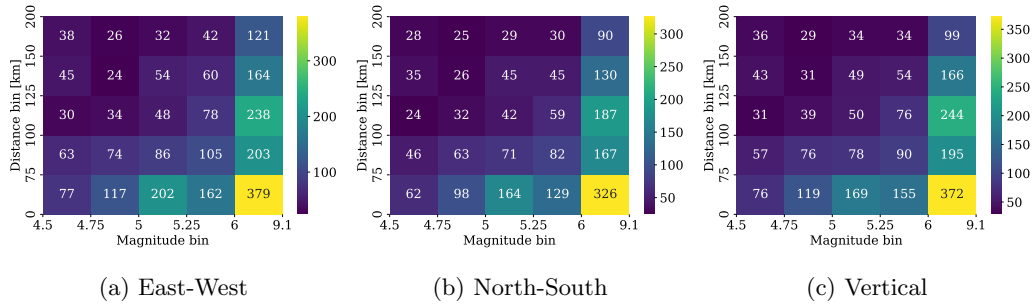


Figure S42: Log-amplitude Fourier spectra Fréchet Distance heatmaps for all three components in different magnitude and distance bins.